Study of relativistic nuclear collisions at AGS energies from p+Be to Au+Au with hadronic cascade model

Y. Nara[1,2], N. Otuka[3], A. Ohnishi[3], K. Niita[1] and S. Chiba[1]

[1] *Advanced Science Research Center, Japan Atomic Energy Research Institute, Tokai, Naka, Ibaraki 319-1195, Japan*

[2] *Physics Department, Brookhaven National Laboratory, Upton, N.Y. 11973, U.S.A.*

[3] *Division of Physics, Graduate School of Science, Hokkaido University, Sapporo 060-0810, Japan*

A hadronic cascade model based on resonances and strings is used to study mass dependence of relativistic nuclear collisions from p+Be to Au+Au at AGS energies ($\sim$ 10AGeV) systematically. Hadron transverse momentum and rapidity distributions obtained with both cascade calculations and Glauber type calculations are compared with experimental data to perform detailed discussion about the importance of rescattering among hadrons. We find good agreement with the experimental data without any change of model parameters with the cascade model. It is found that rescattering is of importance both for the explanation of high transverse momentum tail and for the multiplicity of produced particles.

I. INTRODUCTION

There is now a big interest in studying strongly interacting matter at high density and/or temperature which is created in high energy nuclear collisions. Indeed, at high densities and/or temperatures, QCD predicts the chiral symmetry restoration and quark deconfinement. How can we create such matter ? At present, high energy heavy ion collision is considered to be a unique way to create such dense and hot matter at laboratory. In order to find such a new form of nuclear matter, several heavy ion experiments have been and are being performed with Si(14.6A GeV/c) or Au(11.6A GeV/c) beam at BNL-AGS and with the O(200A GeV/c), S(200A GeV/c) or Pb(158A GeV/c) beam at CERN-SPS.

Since high energy heavy ion collisions lead to a huge number of final states, many event generators have been proposed to explore these high energy nuclear collisions, with the aid of Monte-Carlo realization of complex processes. In these event generators, there are mainly three categories of models. The models in the first category assume Glauber geometry for the treatment of AA collisions. For example, FRITIOF [1], LUCIAE [2], VENUS [3], HIJING [4], DPM [5], HIJET [6] and LEXUS [7] belong to this category. Final interaction among hadrons are included in VENUS, HIJET and LUCIAE. In these models, main quantum features during the multiple scattering are preserved within the eikonal approximation, and efficiently fast calculations are possible. However, these approaches are mainly designed for the extremely high energy collisions ($\sqrt{s} > 10$AGeV).

The models in the second category (parton cascade models), such as VNI [8] and ZPC [9], have been recently developed to implement the interaction among partons to study space-time evolution of partons produced in high energy nuclear collisions. These models have been originally designed to describe ultra-relativistic heavy ion collisions at collider energies, such as BNL-RHIC and CERN-LHC, and they have met some successes in describing heavy ion collisions at CERN-SPS energies [10].

The third category of models is a transport model which is often referred to as 'hadronic cascade'. For example, RQMD [12,13], QGSM [15], ARC [16], ART [17], UrQMD [19] and HSD [18] can be categorized here. They have been successfully used to describe many aspects of high energy heavy ion collisions in a wide range of incident energies. For the description of AA collisions in hadronic cascade models, the trajectories of all hadrons as well as resonances including produced particles are followed explicitly as a function of time. Nuclear collisions are modeled by the sum of independent hadron-hadron (hh) collisions without interferences. Two particles are made to collide if their closest distance is smaller than $\sqrt{\sigma(s)/\pi}$, here $\sigma(s)$ represents the total cross section at the c.m. energy $\sqrt{s}$. As a result of the hh collision, secondary particles will be produced according to the specific model with some formation time. One of the most distinct difference among these models may be in the way of implementing hadronic degrees of freedom. In RQMD and UrQMD, many established hadronic resonances are explicitly propagated in space-time, while ARC, ART and HSD do not include higher hadronic resonances. Although both modelings seem to give similar results if we see the final hadronic spectra inclusively, we expect thermodynamic quantities like pressure or temperature before freeze-out predicted by those models would be different from each other [21]. Another difference is the treatment of multiparticle production. String model is adapted in RQMD, QGSM, UrQMD and HSD, while in ARC and ART, final states are sampled according to the direct parameterization of the experimental data. The hadronic cascade

model based on the string phenomenology implies that some partonic degrees of freedom play some roles in reaction dynamics implicitly. In fact, the estimation of partonic degrees of freedom has been done recently within UrQMD [20]. ARC [16] has shown that 'pure' hadronic model can describe the data at AGS energies. At collider energies, however, explicit treatments of partonic degrees of freedom will be necessary.

The main purpose of this work is to perform systematic analyses of collisions from pA to massive AA systems at AGS energies, for which high-quality systematic experimental data are available [39,40], within the hadronic cascade model, JAM1.0, which has been developed recently based on resonances, strings and pQCD.

The main features included in JAM are as follows. (1) At low energies, inelastic hh collisions are modeled by the resonance productions based on the idea from RQMD and UrQMD. (2) Above the resonance region, soft string excitation is implemented along the lines of the HIJING model [4]. (3) Multiple minijet production is also included in the same way as the HIJING model in which jet cross section and the number of jet are calculated using an eikonal formalism for perturbative QCD (pQCD) and hard parton-parton scatterings with initial and final state radiation are simulated using PYTHIA [22] program. (4) Rescattering of hadrons which have original constituent quarks can occur with other hadrons assuming the additive quark cross section within a formation time. Since these features of the present hadronic cascade model, JAM1.0, enables us to explore heavy ion collisions in a wide energy range, from 100A MeV to RHIC energies, in a unified way, it is a big challenge for us to make systematic analyses in these energies. In this paper, we focus on the mass dependence of the collision system at AGS energies. Other applications at higher energies are found elsewhere [23].

The outline of this paper is as follows. We will present a detailed description of cross sections and modeling of inelastic processes for hh collisions in section II, because elementary hh processes are essential inputs for the hadronic cascade model. In Sec. III, we first study the transverse momentum distributions of protons, pions and kaons in p+Be, p+Al, p+Cu, p+Au, Si+A, Si+Cu and Si+Au collisions at the laboratory incident momentum of 14.6A GeV/c. We discuss the role of rescattering by comparing the cascade model results with the Glauber type calculations. We then discuss the collision dynamics for truly heavy ion colliding system Au+Au collisions. The summary and outlook are given in Sec. IV.

II. MODEL DESCRIPTION

In this section, we present the assumptions and parameters of our model together with the inclusive and the exclusive hh data including incident energy dependence.

A. MAIN COMPONENTS OF THE MODEL

The main components of our model are as follows. (1) Nuclear collision is assumed to be described by the sum of independent binary hh collisions. Each hh collision is realized by the closest distance approach. In this work, no mean field is included, therefore the trajectory of each hadron is straight in between two-body collisions, decays or absorptions. (2) The initial position of each nucleon is sampled by the parameterized distribution of nuclear density. Fermi motion of nucleons are assigned according to the local Fermi momentum. (3) All established hadronic states, including resonances, are explicitly included with explicit isospin states as well as their anti-particles. All of them can propagate in space-time. (4) The inelastic hh collisions produce resonances at low energies while at high energies ($\gtrsim$ 4GeV in BB collisions $\gtrsim$ 3GeV in MB collisions and $\gtrsim$ 2GeV in MM collisions) color strings are formed and they decay into hadrons according to the Lund string model [22]. Formation time is assigned to hadrons from string fragmentation. Formation point and time are determined by assuming yo-yo formation point. This choice gives the formation time of roughly 1 fm/c with string tension $\kappa = 1$GeV/fm. (5) Hadrons which have original constituent quarks can scatter with other hadrons assuming the additive quark cross section within a formation time. The importance of this quark(diquark)-hadron interaction for the description of baryon stopping at CERN/SPS energies was reported by Frankfurt group [12,19]. (6) Pauli-blocking for the final nucleons in two-body collisions are also considered. (7) We do not include any medium effect such as string fusion to rope [3,12], medium modified cross sections and in-medium mass shift. All results which will be presented in this paper are those obtained from the free cross sections and free masses as inputs.

B. Baryon-baryon interactions

Let us start with the explanation of the resonance model for baryon-baryon (BB) collisions implemented in our model in detail. We assume that inelastic BB collisions are described by the resonance formations and their decays below C.M. energy $\sqrt{s} < 4$GeV and at higher colliding energies, string formation and their fragmentation into hadrons are included based on a similar picture to that in the RQMD [13] and the UrQMD model [19]. The total and elastic pp and pn cross sections are well known. Fitted cross sections and experimental data are shown in Fig. 1. Inelastic cross sections are assumed to be filled up with the resonance formations up to $\sqrt{s} =$3-4GeV. At higher energies, the difference between experimental inelastic cross section and resonance formation cross sections are assigned to the string formation.
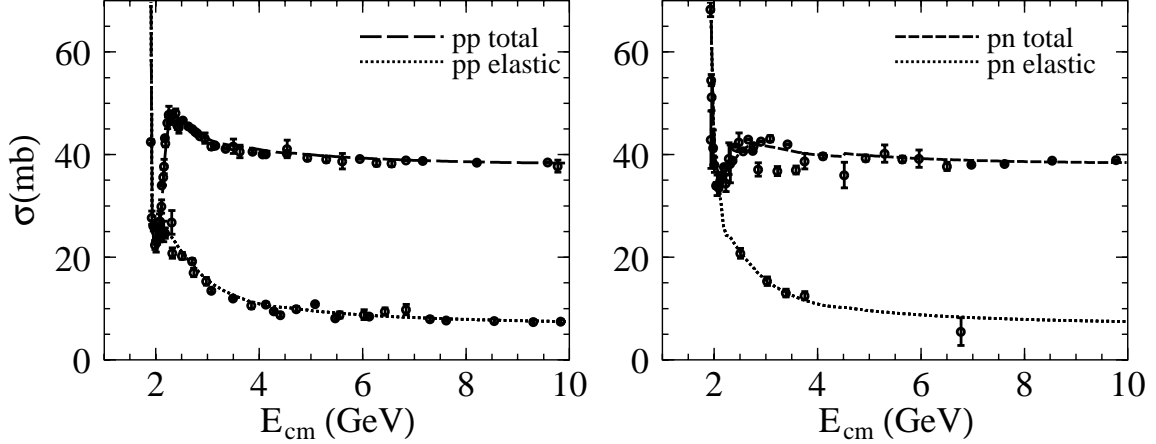

FIG. 1. The fitted total and elastic pp and pn cross sections which are used in the code together with measured data taken from particle data group [24]. CERN-HERA and COMPAS group parameterization are used at high energy [24].

The following non-strange baryonic resonance excitation channels are implemented for the nucleon-nucleon scattering in our model:

(1) $NN \to N\Delta(1232)$, (2) $NN \to NN^*$, (3) $NN \to \Delta(1232)\Delta(1232)$,

(4) $NN \to N\Delta^*$, (5) $NN \to N^*\Delta(1232)$, (6) $NN \to \Delta(1232)\Delta^*$, (7) $NN \to N^*N^*$,

(8) $NN \to N^*\Delta^*$, (9) $NN \to \Delta^*\Delta^*$.

Here N^* and Δ^* represent higher baryonic states below 2 GeV/c^2. The pp and pn cross sections are calculated from each isospin components $\sigma(I)$ (in some cases we ignore the interferences between different amplitudes):

$$\sigma(h_1h_2 \to h_3h_4) = \sum_I |C(h_1h_2, I)|^2 |C(h_3h_4, I)|^2 \sigma(I) \tag{1}$$

where $C(h_ih_j, I)$ is isospin Clebsch-Gordon coefficients. For N^* and Δ^* productions, the sum of production cross sections of several resonance species ($N(1440) \sim N(1990)$ for N^* and $\Delta(1600) \sim \Delta(1950)$ for Δ^*) are parameterized, and resonance species are chosen afterward (see below). The strength of each branches $\sigma(I)$ are determined from the exclusive pion production data [25]. Isospin $I = 1$ component for NN collisions can be extracted from the pp reactions. We assume that isospin $I = 0$ components are determined from the pn reactions, then explicit form of cross sections in different isospin channels can be written down as follows,

$$\sigma(pp \to p\Delta^+) = \frac{1}{4}\sigma(I = 1), \qquad \sigma(pn \to n\Delta^+) = \frac{1}{4}\sigma(I = 1), \tag{2}$$

$$\sigma(pp \to n\Delta^{++}) = \frac{3}{4}\sigma(I = 1), \qquad \sigma(pn \to p\Delta^0) = \frac{1}{4}\sigma(I = 1), \tag{3}$$

$$\sigma(pp \to pp^*) = \sigma(I = 1), \qquad \sigma(pn \to np^*) = \frac{1}{4}\sigma(I = 1) + \frac{1}{4}\sigma(I = 0), \tag{4}$$

$$\sigma(pp \to \Delta^+\Delta^+) = \frac{2}{5}\sigma(I=1), \qquad \sigma(pn \to \Delta^0\Delta^+) = \frac{1}{20}\sigma(I=1) + \frac{1}{4}\sigma(I=0), \tag{5}$$

$$\sigma(pp \to \Delta^0\Delta^{++}) = \frac{3}{5}\sigma(I=1), \qquad \sigma(pn \to \Delta^-\Delta^{++}) = \frac{9}{20}\sigma(I=1) + \frac{1}{4}\sigma(I=0) . \tag{6}$$

The functional form for the non-strange baryonic resonance formation cross sections is assumed to be

$$\sigma(\sqrt{s}) = \frac{\mathrm{a}(\sqrt{s}/\sqrt{s}_{th} - 1)^{\mathrm{b}}\mathrm{d}}{(\sqrt{s}/\mathrm{c} - 1)^2 + \mathrm{d}^2} . \tag{7}$$

All parameters except one-Δ production cross section are listed in tables I and II for each isospin channel where all cross sections are given in mb and $\sqrt{s}_{th}$ denotes a threshold. One-Δ production cross section $\sigma(NN \to N\Delta(1232))$ is parameterized with the following functional form

$$\sigma_1(NN \to N\Delta(1232)) = \frac{0.0052840\sqrt{\sqrt{s}/2.0139999 - 1}}{(\sqrt{s} - 2.11477)^2 + 0.0171405^2} + \frac{28.0401(\sqrt{s}/2.124 - 1)^{0.480085}}{((\sqrt{s}/2.06672) - 1)^2 + 0.576422^2}, \tag{8}$$

in order to ensure correct threshold behavior. Pionic fusion cross section $(pp \to d\pi^+)$ has been fitted as

$$\sigma(pp \to d\pi^+) = \frac{0.14648(\sqrt{s}/2.024 - 1)^{0.20807}}{((\sqrt{s}/2.13072) - 1)^2 + 0.042475^2} + \frac{0.12892(\sqrt{s}/2.054 - 1)^{0.08448}}{((\sqrt{s}/2.18138) - 1)^2 + 0.059207^2}. \tag{9}$$

In actual simulations, we have effectively included the cross section of the $NN \to \pi d$ into the Δ production cross section for simplicity. Similarly the s-wave pion production channels $NN \to NN\pi_s$ are simulated as the $N(1440)$ production.

TABLE I. Resonances cross section parameters for I=1, π_s denotes s-wave pion production.

Channel	a	b	c	d	$\sqrt{s}_{th}$
$\sigma_1(NN \to NN^*)$	24.94700	2.48150	2.63330	0.425358	2.162
$\sigma_1(NN \to \Delta(1232)\Delta(1232))$	7.63181	1.41140	2.67784	0.311722	2.252
$\sigma_1(NN \to N\Delta^*)$	8.01615	2.74161	3.34503	0.259703	2.340
$\sigma_1(NN \to N^*\Delta(1232))$	13.14580	2.06775	2.75682	0.247810	2.300
$\sigma_1(NN \to \Delta(1232)\Delta^*)$	19.63220	2.01946	2.80619	0.297073	2.528
$\sigma_1(NN \to N^*N^*)$	11.67320	2.31682	2.96359	0.259223	2.438
$\sigma_1(NN \to N^*\Delta^*)$	2.99086	2.29380	3.54392	0.090438	2.666
$\sigma_1(NN \to \Delta^*\Delta^*)$	35.13780	2.25498	3.14299	0.215611	2.804
$\sigma_1(NN \to NN\pi_s)$	15.644100	1.675220	2.07706	0.658047	2.014

TABLE II. Resonances cross section parameters for I=0, π_s denotes s-wave pion production.

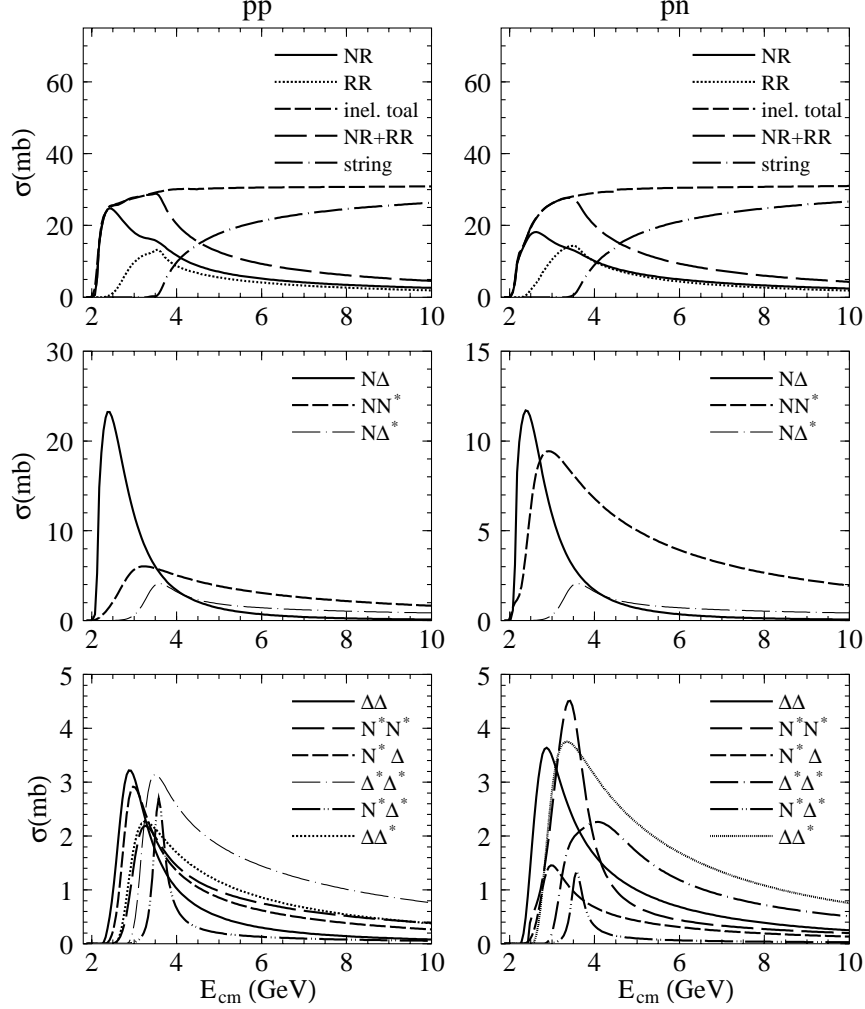| Channel	a	b	c	d	$\sqrt{s}_{th}$
$\sigma_0(NN \to NN^*)$	166.60600	2.10128	2.34635	0.284955	2.162
$\sigma_0(NN \to \Delta(1232)\Delta(1232))$	39.99770	1.83576	2.40348	0.288931	2.252
$\sigma_0(NN \to \Delta(1232)\Delta^*)$	56.32490	2.00679	2.71312	0.362132	2.528
$\sigma_0(NN \to N^*N^*)$	2.14575	0.21662	3.40108	0.252889	2.438
$\sigma_0(NN \to \Delta^*\Delta^*)$	4.14197	1.67026	3.75133	0.476595	2.804
$\sigma_0(NN \to NN\pi_s)$	78.868103	0.746742	1.25223	0.404072	2.014

FIG. 2. The resonance production cross sections for pp (left panels) and pn (right panels) reactions as functions of c.m. energies. In the upper panels, the total one-resonance (NR), double-resonance (RR), total resonance (NR+RR), total inelastic cross section and string formation cross sections are shown. In the middle and the lower panels, each one-resonance production branches and double-resonance production branches are plotted.

In Fig. 2, We show the contributions of non-strange baryonic resonance cross sections for different partial channels as functions of c.m. energies. The upper panels of Fig. 2 show the one-resonance production cross section $NN \to NR$ (solid lines), two-resonance production cross section $NN \to RR$ (dotted lines), the sum of NR and RR cross section (long dashed lines) for pp (left panels) and pn (right panels) reactions. Total inelastic cross sections are filled up by the resonance productions up to about E_{cm} =4GeV, while at CERN/SPS energies, string excitation is dominated. The dot-dashed lines in the upper panels of Fig. 2 express the string excitation cross sections for pp and pn. At AGS energies corresponding to the invariant mass $\sqrt{s} \sim$ 5GeV, the contributions of the resonance productions and string productions are approximately the same in the first nucleon-nucleon collision in our parameterization. The collision spectrum in BB collisions, however, are spread in broad energy range for Au+Au collision as shown in Ref. [19], due to the high baryon density achieved at AGS energies. Low energy cross sections, therefore, is also important in order to treat the dynamics correctly at AGS energies from first chance NN collisions to the final hadronic gas stage.

The cross section for the resonance productions may be written by

$$\frac{d\sigma_{12 \to 34}}{d\Omega} = \frac{(2S_3 + 1)(2S_4 + 1)}{64\pi^2 s p_{12}} \int \int p_{34} |\mathcal{M}|^2 A(m_3^2) A(m_4^2) d(m_3^2) d(m_4^2) , \tag{10}$$

where $S_i, i = 3, 4$ express the spin of the particles in the final state. Mass distribution function $A(m_i)$ for nucleons is

just a δ-function, while that for resonances is given by the relativistic Breit-Wigner function

$$A(m^2) = \frac{1}{\mathcal{N}} \frac{m_R \Gamma(m)}{(m^2 - m_R^2)^2 + m_R^2 \Gamma(m)^2}. \tag{11}$$

where $\mathcal{N}$ denotes the normalization constant. In this paper, we use simply take $\mathcal{N} = \pi$ which is a value in the case of a constant width. The full width $\Gamma(m)$ is a sum of all partial decay width $\Gamma_R(MB)$ for resonance R into mesons M and baryons B which depends on the momentum of the decaying particle [13,19]:

$$\Gamma_R(MB) = \Gamma_R^0(MB) \frac{m_R}{m} \left(\frac{p_{cms}(m)}{p_{cms}(m_R)} \right)^{2\ell+1} \frac{1.2}{1 + 0.2 \left(\frac{p_{cms}(m)}{p_{cms}(m_R)} \right)^{2\ell+1}} \tag{12}$$

where ℓ and $p_{cms}(m)$ are the relative angular momentum and the relative momentum in the exit channel in their rest frame.

The Monte Carlo procedure is as follows. First, final resonance types $\Delta(1232)$, N^* or Δ^* are chosen using parameterized cross sections and then we determine each resonance production channel according to the equation Eq.(10). To do this, we need to know the matrix element $|\mathcal{M}|^2$ for all resonances. In the present model, we make a simple assumption that each resonance production cross sections can be selected according to the probability:

$$P(R_i, R_j) \sim (2S_i + 1)(2S_j + 1) \int \int p_{ij} A_i(m_i^2) A_j(m_j^2) d(m_i^2) d(m_j^2) . \tag{13}$$

Namely, the partial cross section for each resonance state is only governed by the final spins and mass integrals ignoring the resonance state dependence of the matrix element. Once types of resonances are chosen, we generate the resonance masses according to the distribution neglecting the mass dependence of the matrix elements in Eq. (10)

$$P(m_3, m_4) dm_3 dm_4 \sim 4 m_3 m_4 p_{34} A(m_3^2) A(m_4^2) dm_3 dm_4 , \tag{14}$$

in the reaction $1 + 2 \to 3 + 4$, where mass distribution function $A(m_i)$ should be replaced by the δ-function in the case of stable particles in the final state.

In the case of the collisions involving resonance states in the ingoing channel, we use the approximation that the inelastic cross sections for resonance productions as well as the elastic cross section are the same as the nucleon-nucleon cross sections at the same momentum in the c.m. frame, except for de-excitation processes, $NR \to NN$ and $RR \to NN$, whose cross sections are estimated by using the detailed balance described in the next subsection, II C.
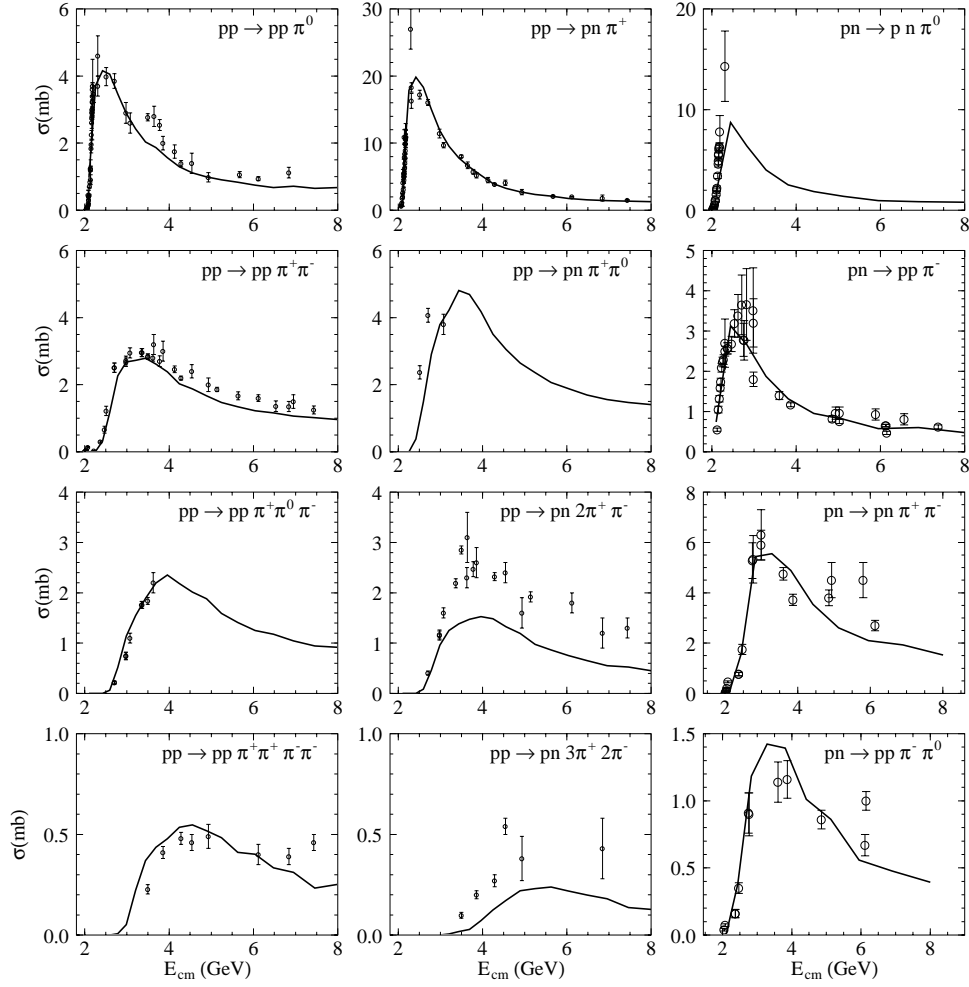
FIG. 3. The energy dependence of the exclusive pion production cross sections for proton-proton and proton-neutron interactions as a function of c.m. energy. Solid lines are the results obtained from the code. Data from Ref. [25].

Fig. 3 shows the energy dependence of the exclusive pion production cross sections in pp (up to five pion production) and pn (up to two pion production) reactions. We compare the results obtained from our simulation with the data [25]. Overall agreement is achieved in these exclusive pion productions within a factor of two with the above simplification of the common matrix element in Eq. (13). Smooth transition from the resonance picture to the string picture at $E_{cm} = 3 \sim 4$ is achieved since no irregularity of the energy dependence is present in the calculated results. String excitation law will be described later in section II E. In order to get more satisfactory fit, for example, we can improve the model by introducing different values for the matrix elements for different resonance channels. For example, in Ref. [27], the matrix elements are fitted to reproduce the pion production cross sections up to two-pion productions as well as η production cross section assuming that they are independent of masses but dependent on species.

C. Detailed balance

In the processes of resonance absorption, we use a generalized detailed balance formula [28–30] which takes the finite width of the resonance mass into account. The time-reversal invariance of the matrix element leads to the principle of detailed balance. If scattering particles are all stable, the formula is given by

$$\frac{d\sigma_{34\to12}}{d\Omega} = \frac{(2S_1+1)(2S_2+1)}{(2S_3+1)(2S_4+1)} \frac{p_{12}^2}{p_{34}^2} \frac{d\sigma_{12\to34}}{d\Omega} \tag{15}$$

where S_i denotes the spin of particle i and p_{ij} corresponds to the c.m. momentum of the particles i and j.

The differential cross section for the reaction $(1,2)\to(3,4)$ for the stable particles may be written by

$$\frac{d\sigma_{12\to34}}{d\Omega} = \frac{|\mathcal{M}_{12\to34}|^2}{64\pi^2 s} \frac{1}{(2S_1+1)(2S_2+1)} \frac{1}{p_{12}} \int\int p_{34}\, \delta(p_3^2 - m_3^2)d(m_3^2)\delta(p_4^2 - m_4^2)d(m_4^2) \tag{16}$$

where $|\mathcal{M}_{12\to34}|^2$ represents the spin-averaged matrix element. If the particles have a finite width, we should replace above δ functions to the certain normalized mass distribution functions $A(m)$. Using the $|\mathcal{M}_{12\to34}| = |\mathcal{M}_{34\to12}|$, we obtain

$$\frac{d\sigma_{34\to12}}{d\Omega} = \frac{(2S_1+1)(2S_2+1)}{(2S_3+1)(2S_4+1)} \frac{p_{12}^2}{p_{34}} \frac{d\sigma_{12\to34}}{d\Omega} \frac{1}{\int\int p_{34} A(m_3^2)A(m_4^2)d(m_3^2)d(m_4^2)}\ , \tag{17}$$

where we use the relativistic Breit-Wigner function Eq.(11) for mass distribution function $A(m^2)$. The extra factor compared to the usual detailed balance formula increases the absorption cross section. It has been proved that this formula plays an essential role in order to understand the $\pi N\Delta$ dynamics [28–30].

In the case of one-$\Delta(1232)$ absorption cross section, we can write down the following formula:

$$\sigma_{N\Delta\to NN'} = \frac{1}{2} \frac{1}{1+\delta_{NN'}} \frac{p_N^2}{p_\Delta} \sigma_{NN'\to N\Delta} \left(\int_{(m_N+m_\pi)^2}^{(\sqrt{s}-m_N)^2} p_{\Delta(1232)} A(m^2)dm^2 \right)^{-1}. \tag{18}$$

p_N and p_Δ are the final nucleon-nucleon c.m. momentum and the initial c.m. momentum, respectively. The factor $1/(1+\delta_{NN'})$ in Eq.(18) arises from the identical nature of the final states, and $1/2$ comes from spins.

There are some versions of the extended detailed balance formula, which are slightly different from each other. For example, Danielewicz and Bertch [28] use the formula

$$\frac{d\sigma_{34\to12}}{d\Omega} = \frac{(2S_1+1)(2S_2+1)}{(2S_3+1)(2S_4+1)} \frac{p_{12}^2}{p_{34}} \frac{m_3}{m_3^R} \frac{m_4}{m_4^R} \frac{d\sigma_{12\to34}}{d\Omega} \frac{1}{\int\int p_{34} A(m_3'^2)A(m_4'^2)dm_3'^2 dm_4'^2}, \tag{19}$$

here m_i^R denotes the pole mass of the resonance i, while Wolf, Cassing and Mosel [30] use

$$\frac{d\sigma_{34\to12}}{d\Omega} = \frac{(2S_1+1)(2S_2+1)}{(2S_3+1)(2S_4+1)} \frac{p_{12}^2}{p_{34}^2} \frac{d\sigma_{12\to34}}{d\Omega} \frac{1}{\int\int A(m_3^2)A(m_4^2)dm_3^2 dm_4^2}. \tag{20}$$

We have checked that these formulae give similar results to ours. Fig. 4 shows the comparisons between the different formulae of the cross sections for the reaction $\Delta^{++}n \to pp$.
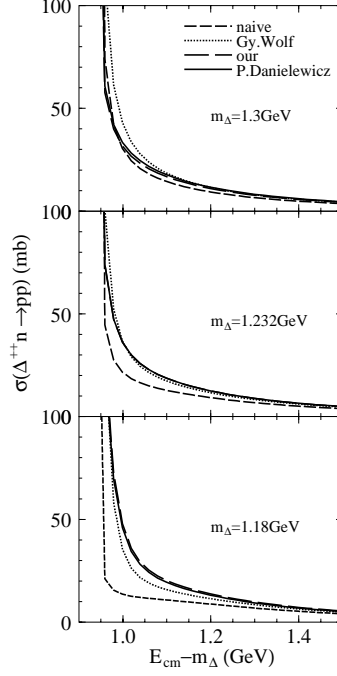
FIG. 4. The cross section for $\Delta^{++}n \to pp$ calculated using the different descriptions for the detailed balance as a function of $\sqrt{s} - M_\Delta$, where M_Δ is the mass of ingoing Δ. The short-dashed lines correspond to the results of the formula which does not take the Δ width into account. The results of the cross sections obtained using the formula in Ref. [30] and [28] are shown by dotted and full lines respectively. The long-dashed lines correspond to the results using Eq.(18).

D. Meson-Baryon, Meson-Meson Collisions

We now turn to the explanation of meson-baryon (MB) and meson-meson (MM) collisions. We also use resonance/string excitation model for MB and MM collisions.
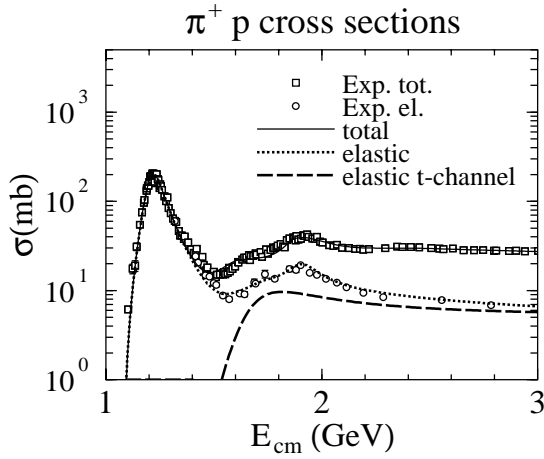
FIG. 5. Parameterization of the total and elastic π^+p cross sections. The data has been taken from [24]. Total and elastic cross sections are assumed to be the sum of s-channel and t-channel resonance and/or string formation processes.
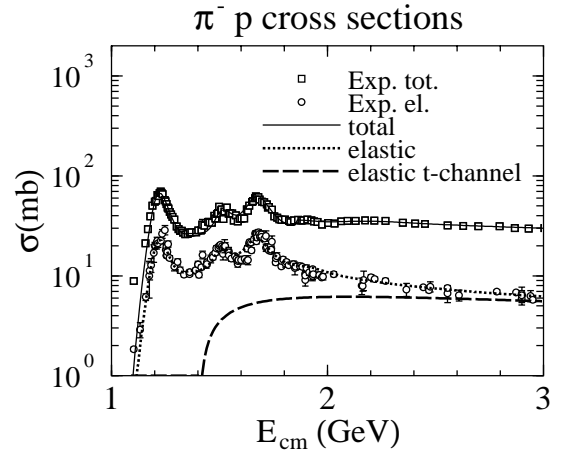
FIG. 6. Parameterization of the total and elastic π^-p cross sections. The data has been taken from [24].

9

Total cross section for πN ingoing channel is assumed to be decomposed to

$$\sigma_{tot}(s)^{\pi N} = \sigma_{BW}(s) + \sigma_{el}(s) + \sigma_{\text{S-S}}(s) + \sigma_{\text{t-S}}(s), \tag{21}$$

where $\sigma_{el}(s)$, $\sigma_{BW}(s)$, $\sigma_{\text{S-S}}(s)$, and $\sigma_{\text{t-S}}(s)$ denote the t-channel elastic cross section, the s-channel resonance formation cross section with the Breit-Wigner form, the s-channel and t-channel string formation cross sections, respectively. We neglect the t-channel resonance formation cross section at a energy range of $\sqrt{s} \lesssim 2\text{GeV}$. The t-channel elastic cross section $\sigma_{el}(s)$ was determined so that the sum of the elastic component of the s-channel Breit-Wigner cross section $\sigma_{BW}(s)$ and t-channel elastic cross section $\sigma_{el}(s)$ reproduces the experimental elastic data for πN interaction. Above the $\Delta(1232)$ region, t-channel elastic cross section becomes non-zero in our parameterization (Figs. 5 and 6). String formation cross sections ($\sigma_{\text{S-S}}(s)$ and $\sigma_{\text{t-S}}(s)$) are determined to fill up the difference between experimental total cross section and $\sigma_{BW}(s) + \sigma_{el}(s)$. We calculate the resonance formation cross section $\sigma_{BW}(s)$ using the Breit-Wigner formula [37,12] (neglecting the interference between resonances),

$$\sigma(MB \to R) = \frac{\pi(\hbar c)^2}{p_{cm}^2} \sum_R |C(MB,R)|^2 \frac{(2S_R+1)}{(2S_M+1)(2S_B+1)} \frac{\Gamma_R(MB)\Gamma_R(tot)}{(\sqrt{s}-m_R)^2 + \Gamma_R(tot)^2/4} . \tag{22}$$

The momentum dependent decay width Eq. (12) are also used for the calculation of decay width in Eq. (22). S_R, S_B and S_M denote the spin of the resonance, the decaying baryon and meson respectively. The sum runs over resonances, $R = N(1440) \sim N(1990)$ and $\Delta(1232) \sim \Delta(1950)$. Actual values for these parameters are taken from the Particle Data Group [24] and adjusted within an experimental error bar to get reasonable fit for MB cross sections. The results of the fit are shown in Figs. 5,6. It has been shown that inclusion of resonances play an important role to study strangeness productions in AGS and SPS energies [12] and (K^-, K^+) reactions [31]. In fact, strangeness production cross sections for resonance-N ingoing channels are found to be much larger than that for πN channel. This would be effective to explain the strangeness enhancement observed in heavy ion collisions within a rescattering scenario.
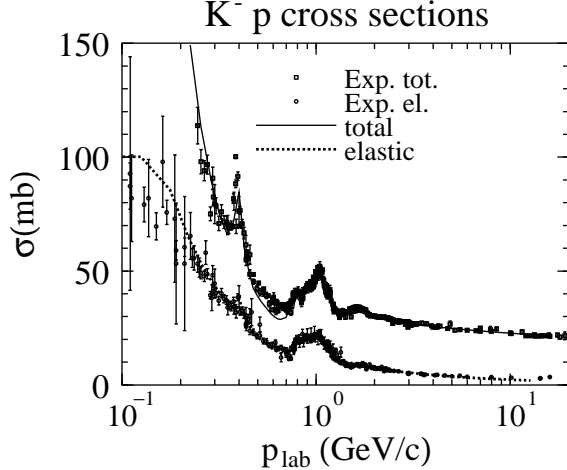

FIG. 7.   Parameterization of the total and elastic K^-p cross sections. The data has been taken from [24]. The sum of the s-channel resonance productions and t-channel elastic, t-channel charge exchange and t-channel hyperon production cross sections can describe the data properly at low energies.
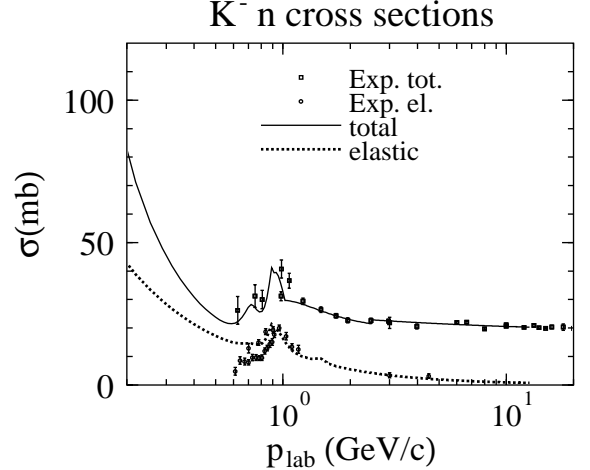
FIG. 8.   Parameterization of the total and elastic K^-n cross sections. Parameterizations of low energy part of the cross section where data is absent are addressed by Ref. [33]. The data has been taken from [24].

Since the $\bar{K}N$ interaction has some exoergic channels such as $\bar{K}N \to \pi Y$, we need to include additional terms:

$$\sigma_{tot}(s)^{\bar{K}N} = \sigma_{BW}(s) + \sigma_{el}(s) + \sigma_{\text{ch}}(s) + \sigma_{\pi Y}(s) + \sigma_{\text{S-S}}(s) + \sigma_{\text{t-S}}(s), \tag{23}$$

where $\sigma_{\text{ch}}(s)$ and $\sigma_{\pi Y}(s)$ denote t-channel charge exchange reaction and t-channel hyperon production cross sections which are also fixed by the requirement that the sum of t-channel contributions and Breit-Wigner contributions reproduce experimental data. Breit-Wigner formula enables us to calculate experimentally unmeasured cross sections

such as $\rho N \to \Lambda K$. For the calculation of $\sigma_{BW}(s)$, we include hyperon resonances, $R = \Lambda(1405) \sim \Lambda(2110)$ and $\Sigma(1385) \sim \Sigma(2030)$. The total and elastic cross sections for $\bar{K}N$ interactions used in JAM are plotted in Figs. 7 and 8 in comparison with experimental data [24].
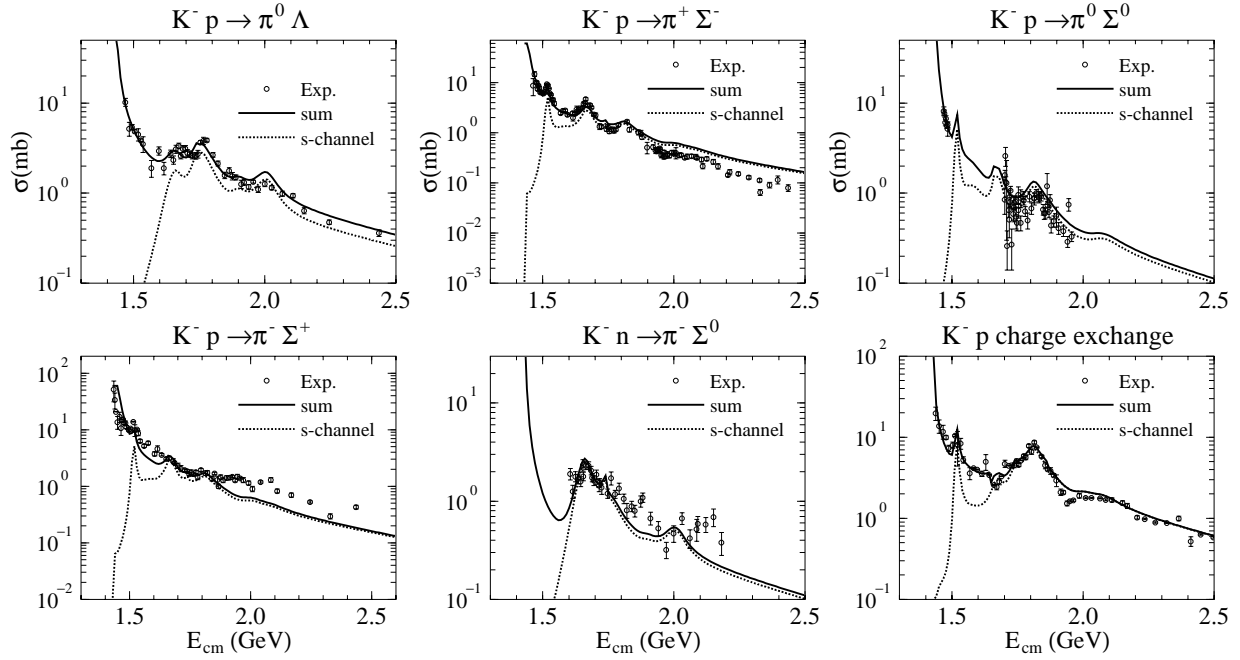

FIG. 9. The energy dependence of the exclusive hyperon production cross sections $K^-p \to \pi^0\Lambda$, $K^-p \to \pi^-\Sigma^+$, $K^-p \to \pi^+\Sigma^-$, $K^-n \to \pi^-\Sigma^0$, $K^-n \to \pi^0\Sigma^0$, and charge exchange cross section $K^-p \to K^0n$ used in the model are shown by the full lines together with s-channel (dotted) contributions. Circles are data from Ref. [26].

The symbol $\sigma_{\pi Y}(s)$ in Eq.(23) is the sum of t-channel pion hyperon production cross sections $\bar{K}N \to \pi Y$, $Y = \Lambda, \Sigma$. In Fig. 9, we plot the cross sections of hyperon productions and charge exchange cross sections as well as Breit-Wigner contributions fitted in our model. The cross section for the inverse processes such as $\pi Y \to \bar{K}N$ are calculated using the detailed balance formula.
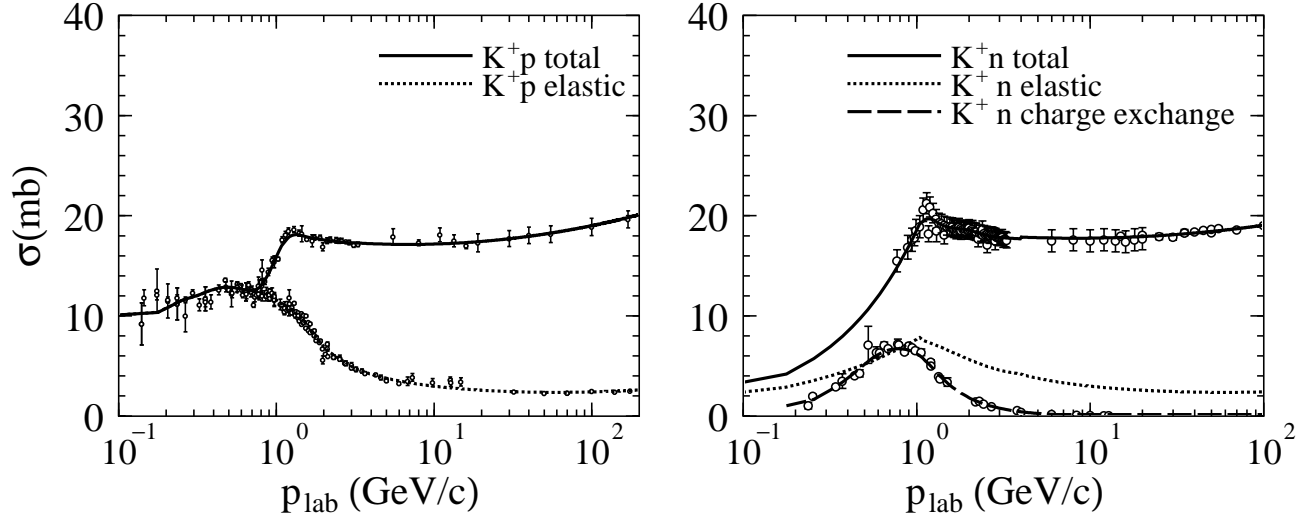
FIG. 10. Parameterization of the total and elastic K^+p and K^+n cross sections as well as charge exchange cross section in K^+n interaction. The data has been taken from [24].

KN ingoing channel cannot form any s-channel resonance due to their quark contents. Therefore the total cross section can be written within our model as follows,

$$\sigma_{tot}(s)^{KN} = \sigma_{\text{t-R}}(s) + \sigma_{el}(s) + \sigma_{\text{ch}}(s) + \sigma_{\text{t-S}}(s), \tag{24}$$

where $\sigma_{\text{t-R}}(s)$ is t-channel resonance formation cross section. Total, elastic and charge exchange cross sections used in our model are shown in Fig. 10. In the present version of JAM, only $KN \to K\Delta$, $KN \to K(892)N$ and $KN \to K(892)\Delta$ are explicitly fitted to experimental data [25] and fitted results are shown in Fig. 11.
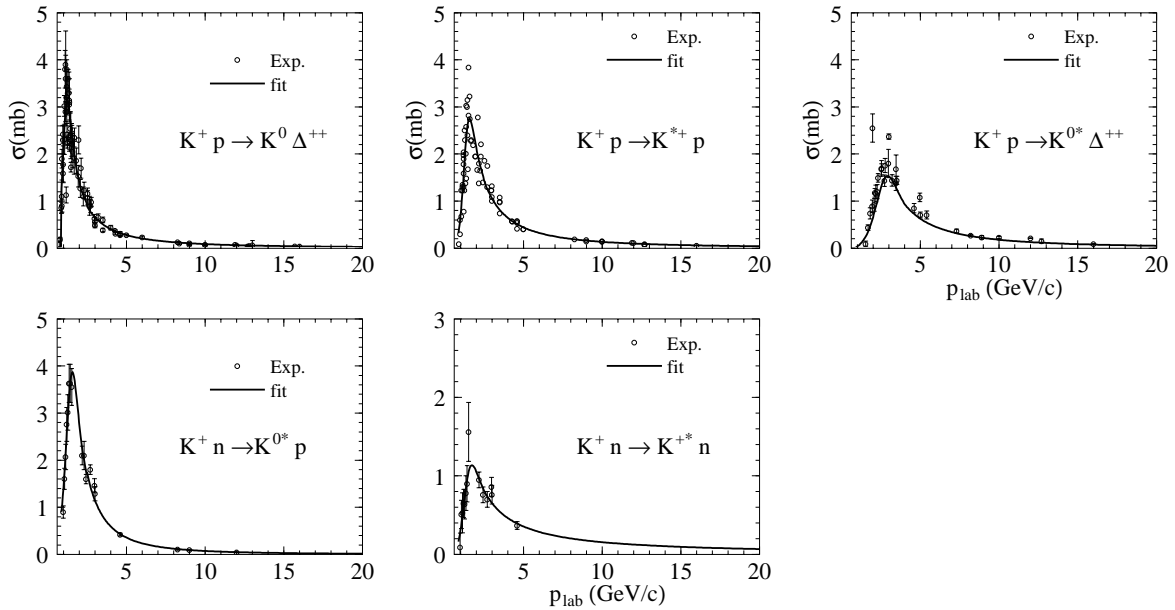

FIG. 11. Parameterization of the Δ, K^* productions cross sections in K^+p and K^+n interactions. The data from Ref. [25].

12

In meson-meson scattering, we also apply the same picture as that in meson-baryon collisions:

$$\sigma_{tot}(s) = \sigma_{BW}(s) + \sigma_{\text{t-R}}(s) + \sigma_{el}(s) + \sigma_{\text{s-S}}(s) + \sigma_{\text{t-S}}(s). \tag{25}$$

The difference between experimental inelastic cross section and resonance cross sections at energies above resonance region for the meson-baryon and meson-meson collisions are attributed to the string formation cross section where $1/\sqrt{s}$ energy dependence of $\sigma_{\text{s-S}}(s)$ is used [13].

For the cross sections for which no experimental data are available, we calculate the total and elastic cross sections by using the additive quark model [32,12,19].

$$\sigma_{tot} = \sigma_{NN} \left(\frac{n_1}{3} \right) \left(\frac{n_2}{3} \right) \left(1 - 0.4 \frac{n_{s1}}{n_1} \right) \left(1 - 0.4 \frac{n_{s2}}{n_2} \right) , \tag{26}$$

$$\sigma_{el} = \sigma_{tot}^{2/3} (\sigma_{el}^{NN} / \sigma_{NN}^{2/3}) , \tag{27}$$

where σ_{NN}, σ_{el}^{NN} express nucleon-nucleon total and elastic cross sections and n_i, n_{si} are the number of quarks and s-quarks contained in the hadron respectively. This expression works well above resonance region where the cross section becomes flat.

For the t-channel resonance production cross sections $\sigma_{\text{t-R}}(s)$, we do not fit experimental data explicitly in this work except for NN reaction and one and two pion productions in KN reaction, because of the vast body of the possibilities for the final states. Instead, we simply determine the outgoing resonance types according to the spins S_3, S_4 in the final state and phase space for the production of resonances R_3 and R_4

$$P(R_3, R_4) \propto (2S_3 + 1)(2S_4 + 1) p_{34}(s)^2 . \tag{28}$$

where $p_{34}(s)$ denotes the c.m. momentum in the final state. If the ingoing channel involves resonances, their ground state particles are also considered in the final state. Once the outgoing resonance types are determined, we generate masses according to the Breit-Wigner distribution.

For the angular dependence in the processes of t-channel resonance production $\sigma_{\text{t-R}}(s)$, we use

$$\frac{d\sigma_{\text{t-R}}(s)}{dt} \sim \exp(bt), \tag{29}$$

and the slope parameter b for the energy range of $\sqrt{s} > 2.17\text{GeV}$ is parameterized by

$$b = 2.5 + 0.7 \log(s/2), \tag{30}$$

with invariant mass squared s given in units of GeV^2. We use the same parameterization presented in Ref. [34] for the energy below $\sqrt{s} < 2.17\text{GeV}$ for the t-channel resonance productions. The elastic angular distribution is also taken from Ref. [34] for $\sqrt{s} < 10\text{GeV}$ and from PYTHIA [22] for $\sqrt{s} > 10\text{GeV}$.

E. String formation and fragmentation

At an energy range above $\sqrt{s} > 4 - 5\text{GeV}$, the (isolated) resonance picture breaks down because width of the resonance becomes wider and the discrete levels get closer. The hadronic interactions at the energy range 4-5$< \sqrt{s} <$10-100GeV where it is characterized by the small transverse momentum transfer is called "soft process", and string phenomenological models are known to describe the data for such soft interaction well. The hadron-hadron collision leads to a string like excitation longitudinally. In actual description of the soft processes, we follow the prescription adopted in the HIJING model [4], as described below.

In the center of mass frame of two colliding hadrons, we introduce light-cone momenta defined by

$$p^+ = E + p_z, \qquad p^- = E - p_z . \tag{31}$$

Assuming that beam hadron 1 moves in the positive z-direction and target hadron 2 moves negative z-direction, the initial momenta of the both hadrons are

$$p_1 = (p_1^+, p_1^-, 0_T), \qquad p_2 = (p_2^+, p_2^-, 0_T) . \tag{32}$$

After exchanging the momentum $(q^+, q^-, \boldsymbol{p}_T)$, the momenta will change to

13

$$p'_1 = ((1 - x^+)P^+, x^- P^-, \boldsymbol{p}_T), \qquad p'_2 = (x^+ P^+, (1 - x^-)P^-, -\boldsymbol{p}_T), \tag{33}$$

where $P^+ = p_1^+ + p_2^+ = P^- = p_1^- + p_2^- = \sqrt{s}$ (in c.m. frame). The string masses will be

$$M_1^2 = x^-(1 - x^+)s - p_T^2, \qquad M_2^2 = x^+(1 - x^-)s - p_T^2, \tag{34}$$

respectively. Minimum momentum fractions are $x_{min}^+ = p_2^+/P^+$ and $x_{min}^- = p_1^-/P^-$. For light-cone momentum transfer for the non-diffractive events, we use the same distribution as that in DPM [5] and HIJING [4]:

$$P(x^\pm) = \frac{(1.0 - x^\pm)^{1.5}}{(x^{\pm 2} + c^2/s)^{1/4}} \,, \tag{35}$$

for baryons and

$$P(x^\pm) = \frac{1}{(x^{\pm 2} + c^2/s)^{1/4}((1 - x^\pm)^2 + c^2/s)^{1/4}} \,, \tag{36}$$

for mesons, where $c = 0.1\text{GeV}$ is a cutoff. For single-diffractive events, in order to reproduce experimentally observed mass distribution dM^2/M^2, we use the distribution

$$P(x^\pm) = \frac{1}{(x^{\pm 2} + c^2/s)^{1/2}}. \tag{37}$$

The strings are assumed to hadronize via quark-antiquark or diquark-antidiquark creation using Lund fragmentation model PYTHIA6.1 [22]. Hadron formation points from a string fragmentation are assumed to be given by the yo-yo formation point [35] which is defined by the first meeting point of created quarks. Yo-yo formation time is about 1fm/c assuming the string tension $\kappa = 1$ GeV/fm at AGS energies.

The same functional form as the HIJING model [4] for the soft $\boldsymbol{p}_T$ transfer at low $p_T < p_0$ is used

$$f(\boldsymbol{p}_T) = \left\{ (p_T^2 + c_1^2)(p_T^2 + p_0^2)(1 + e^{(p_T - p_0)/c_2}) \right\}^{-1} \,, \tag{38}$$

where $c_1 = 0.1\text{GeV/c}$, $p_0 = 1.4\text{GeV/c}$ and $c_2 = 0.4\text{GeV/c}$, to reproduce the high momentum tail of the particles at energies $E_{lab} = 10 \sim 20\text{GeV}$.
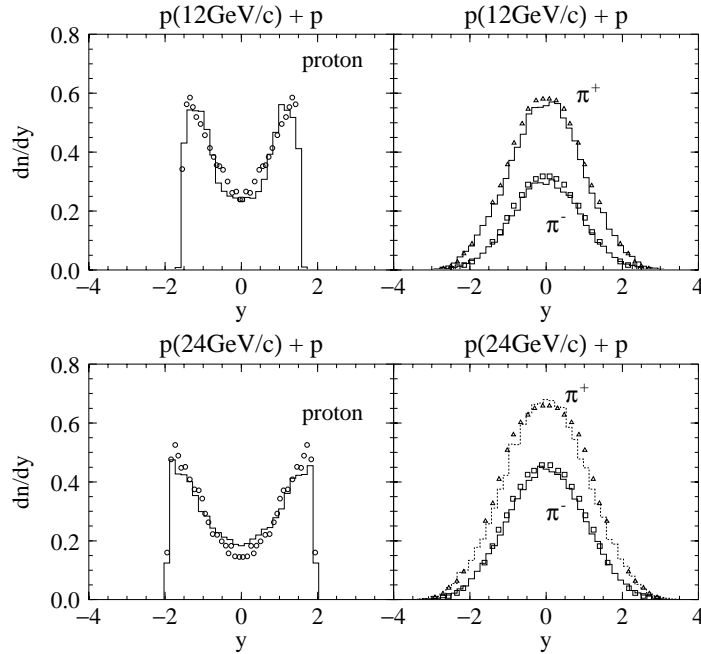

FIG. 12. The rapidity distributions for protons (circles), π^+ (triangles) and π^- (squares) in pp collisions at 12GeV/c (upper panel) and 24GeV/c (lower panel). Histograms are the results obtained from our calculation. The data are from Ref. [36].

14

In Fig. 12, the calculated rapidity distributions of protons, positive and negative pions for proton-proton collisions at 12GeV/c and 24GeV/c are shown with the data from Ref. [36]. The proton stopping behavior and the pion yields are well described by the present model. Within our model, fast protons come from resonance decays and mid-rapidity protons from string fragmentation of Lund model (PYTHIA6.1 [22]) with the default parameter which determines the probability of diquark breaking at these energies. Anisotropic angular distribution in a resonance decay is taken into account assuming Gaussian p_T distribution [13] with a mean value of 0.35GeV/c^2.
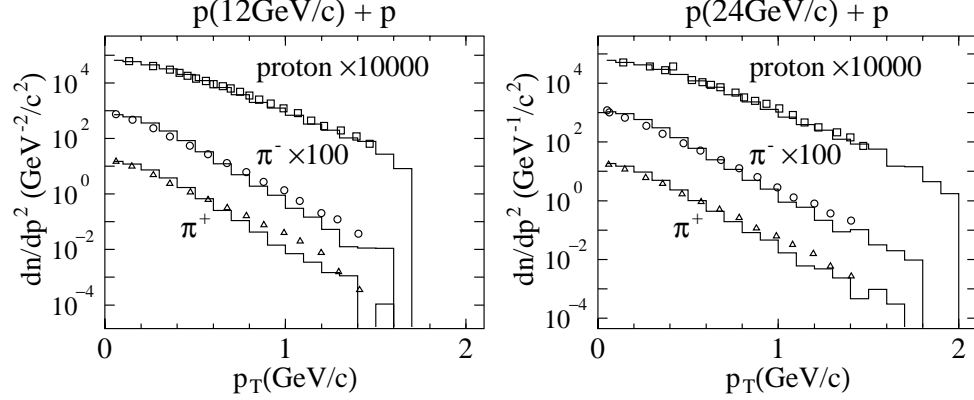
FIG. 13. The transverse momentum distributions for protons (squares), π^+ (triangles) and π^- (circles) in pp collisions at 12GeV/c(left panel) and 24GeV/c(right panel). Histograms are the results obtained from our calculation. The data are from Ref. [36].

As reported in HIJING [4], an extra low p_T transfer to the constituent quarks is important to account for the high p_T tails of the pion and proton distributions at energies $p_{\text{lab}} \sim 20 \text{GeV/c}^2$. As shown in Fig. 13, the present model also reproduces the proton and pion transverse momentum distributions reasonably well at $p_{\text{lab}} = 12 \text{GeV/c}^2$ and 24 GeV/c^2.
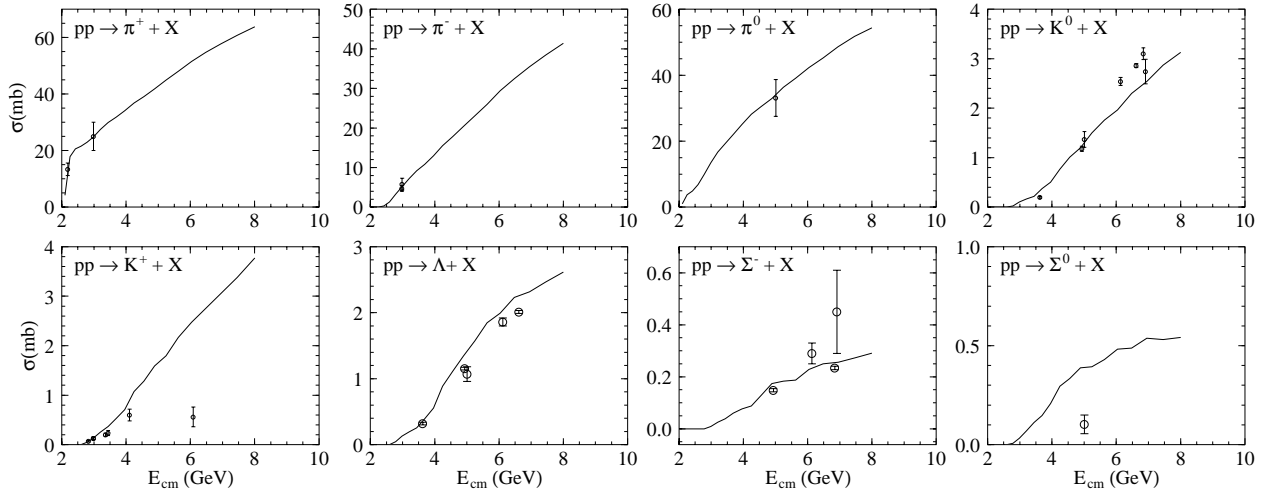

FIG. 14. The energy dependence of the inclusive production cross sections for pions hyperons, kaons for proton-proton interaction as functions of c.m. energy. Solid lines are the results obtained from our model. Data from Ref. [25].

In addition, the present model also describes well the energy dependence of the particle production cross sections,

as shown in Fig. 14. Here we show the incident energy dependence of the inclusive data for π^+, π^-, π^0, K^0,K^+,Λ, Σ^- and Σ^0 productions from proton-proton interactions in comparison with the experimental data [25].

The comparisons shown until now in Figs.2 – 13 show that the combination of particle production mechanisms by the resonance decay and the string decay enables us to explore a wide incident energy region from a few hundred MeV to a few ten GeV, with reasonably well fitted inclusive as well as exclusive cross sections, which are essential inputs in cascade models.

III. RESULTS

In the following, we systematically apply our hadronic cascade model (JAM1.0 [38]) to proton, silicon and gold induced reactions at AGS energies and investigate the effect of cascading by comparing the results obtained by the cascade model with the Glauber type calculations.

A. COMPARISON TO E802 DATA

In this section, we first focus our attention on the proton transverse distributions to check the detailed examination of the collision term and its space-time picture (formation time) used in our model and also to see the transition of the reaction dynamics from proton induced collisions to heavy ion collisions.
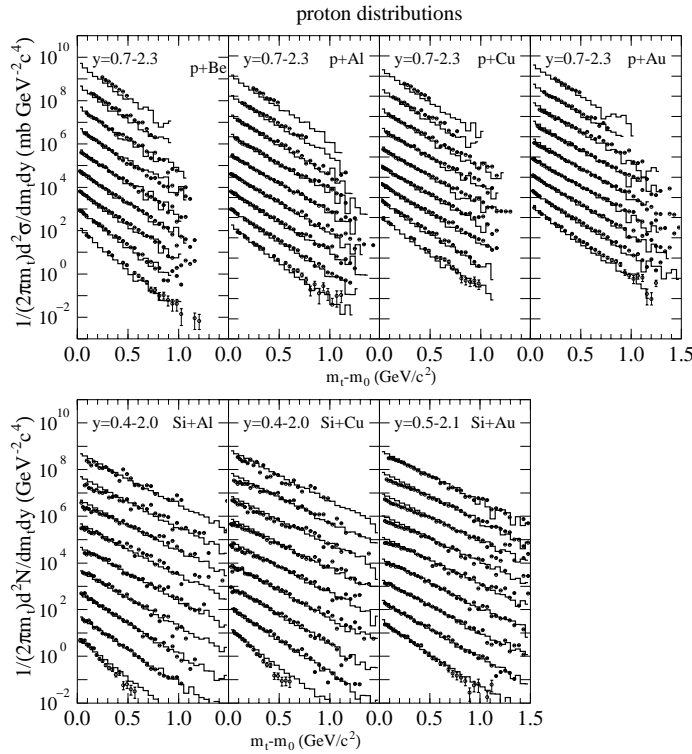

FIG. 15. Invariant cross sections of protons from p+Be, p+Al, p+Cu, p+Au and central Si+Al ($b \leq 1.79$fm), Si+Cu ($b \leq 2.2$fm), and Si+Au ($b \leq 2.9$fm), collisions at 14.6GeV/c. The calculated results from Cascade model (histogram) are compared with the E802 data from Ref. [39,40]. For proton induced collisions (upper panel), rapidity interval is $y = 0.7$ (bottom spectrum) to $y = 2.3$ (top spectrum) with $\delta y = 0.2$. For Si+Al and Si+Cu collisions, rapidity interval is $y = 0.4$ to $y = 2.0$ with $\delta y = 0.2$. For Si+Au collisions, rapidity interval is $y = 0.4$ to $y = 2.0$ with $\delta y = 0.2$. The spectra are increased by a factor of 10 from bottom to upper.

We show in Fig. 15 proton invariant transverse mass distributions calculated by our cascade model for the proton induced reactions, p+Be, p+Al, p+Cu, p+Au, and silicon induced reactions, central Si+Al, Si+Cu, Si+Au at 14.6GeV/c in comparison to the data from the E802 collaboration [39,40]. In each figure, spectra are plotted in a rapidity interval of 0.2 and are displayed by multiplying each by a power of 10 from bottom to upper. Si+Al, Si+Cu and Si+Au data correspond to the central collision with 7 % centrality. For the calculations of Si+A (A=Al,Cu,Au) systems, impact parameter are distributed $b < 1.797$fm for Si+Al, $b < 2.2$fm for Si+Cu and $b < 2.9$fm for Si+Au. Our calculations show good agreement with the data in proton induced reactions. In silicon induced reactions, our

calculations well account for the experimental data in general. However, we can see some overestimate at low transverse momenta, in particular for Si+Au system. As a result, our cascade model gives larger proton stopping than the data.
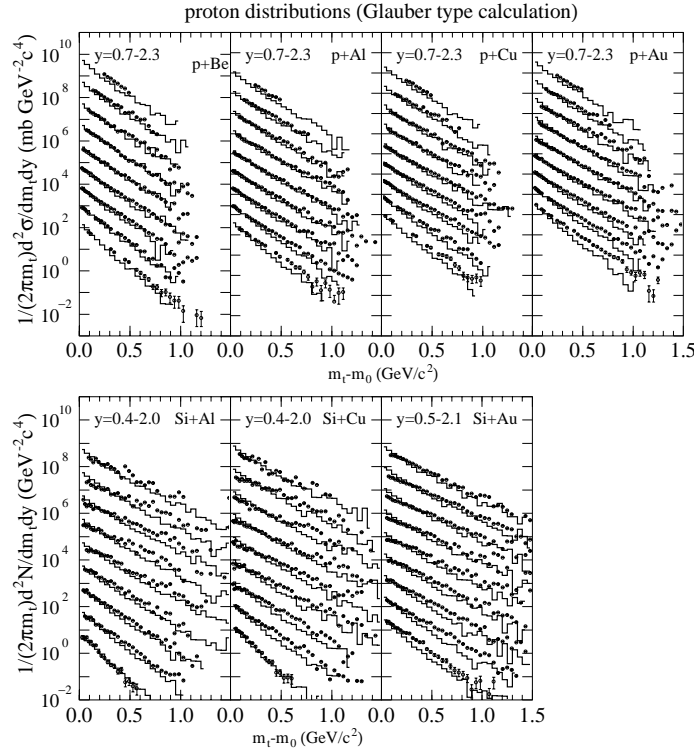

FIG. 16. The Glauber type calculations compared to the data [39,40]. The meaning of the figure is the same as Fig. 15.

Now we compare the cascade model results with the Glauber type calculation in order to see the effect of pion rescattering, nucleon cascading, and the consequent deviation from the linear extrapolation of sum of binary nucleon-nucleon collisions to proton-nucleus and nucleus-nucleus collisions. The Glauber type models such as the FRITIOF model [1] have been widely used at higher energies, i.e. more than 200 AGeV. We use the same method as the FRITIOF model with some modifications. The wounded nucleons become resonances or strings in each nucleon-nucleon collisions, and strings can interact again before they fragment. Resonances can be converted to nucleons, and strings are allowed to be de-excited to the minimum string mass. After all binary collisions are completed, strings and resonances are forced to decay. Rescattering of produced particles are not considered. In a present treatment, we have used our parameterization in calculating the probability to excite nucleons to resonances or strings. Figure 16 shows the results obtained by this Glauber type calculation. In beam rapidity region, for all systems, good agreements can be seen because the effect of rescattering would be small as expected. For proton-induced reactions, the Glauber type calculation gives steeper shape in comparison to the data at mid-rapidity and target regions. In heavy ion reactions, this deviation is significant at around the mid-rapidity. Rescattering, therefore, is necessary to account for transverse momentum distributions of protons for reactions involving heavy nuclei.
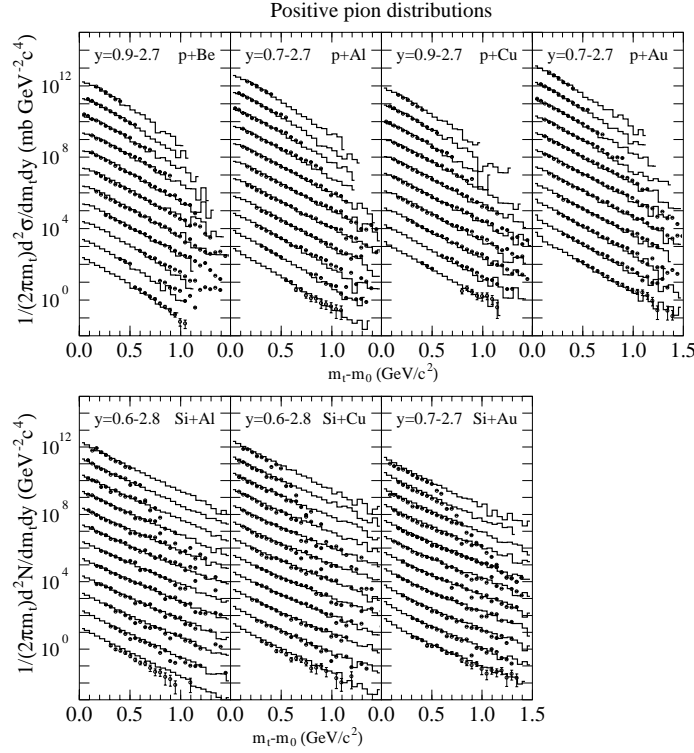
Positive pion distributions

FIG. 17. Invariant cross sections of positive pions from p+Be ($0.9 \leq y \leq 2.7$), p+Al ($0.7 \leq y \leq 2.7$), p+Cu ($0.9 \leq y \leq 2.7$), p+Au ($0.7 \leq y \leq 2.7$), Si+Al ($0.6 \leq y \leq 2.8$), Si+Cu ($0.6 \leq y \leq 2.8$) and Si+Au ($0.7 \leq y \leq 2.7$) collisions at 14.6GeV/c. The calculated results from cascade model (histogram) are compared with the E802 data from Ref. [39,40]. The bin of rapidity is 0.2 for all collision systems. The spectra are increased by a factor of 10 from bottom to upper.

Negative pion distributions
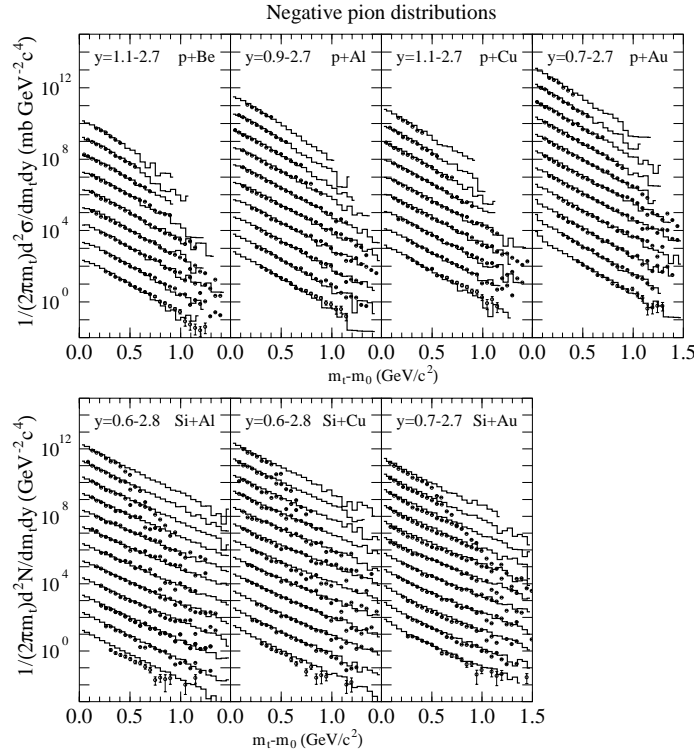
FIG. 18. Invariant cross sections of negative pions from p+Be ($1.1 \leq y \leq 2.7$), p+Al ($0.9 \leq y \leq 2.7$), p+Cu ($1.1 \leq y \leq 2.7$), p+Au ($0.7 \leq y \leq 2.7$), Si+Al ($0.6 \leq y \leq 2.8$), Si+Cu ($0.6 \leq y \leq 2.8$) and Si+Au ($0.7 \leq y \leq 2.7$) collisions at 14.6GeV/c. The calculated results from Cascade model (histogram) are compared with the E802 data from Ref. [39,40]. The bin of rapidity is 0.2 for all collision systems. The spectra are increased by a factor of 10 from bottom to upper.

18

We now turn to the mass dependence of the pion transverse distributions. In Fig. 17 and Fig. 18, we show the calculated π^+ and π^- spectra by histograms together with the E802 data [39,40]. Agreement between the cascade model and the data is very good for all the combination of projectile and target, and for both of the slope parameter and the absolute value of the cross section.

On the other hand, as shown in Fig. 19 and Fig. 20, Glauber type calculations well reproduce the data for small mass systems p+Be, p+Al, p+Cu and Si+Al, and give similar slopes to the experimental data, while the multiplicity of pions in heavy systems are larger than those of the data. This is due to the effect of rescattering in which pions are absorbed during the evolution for the large mass systems.
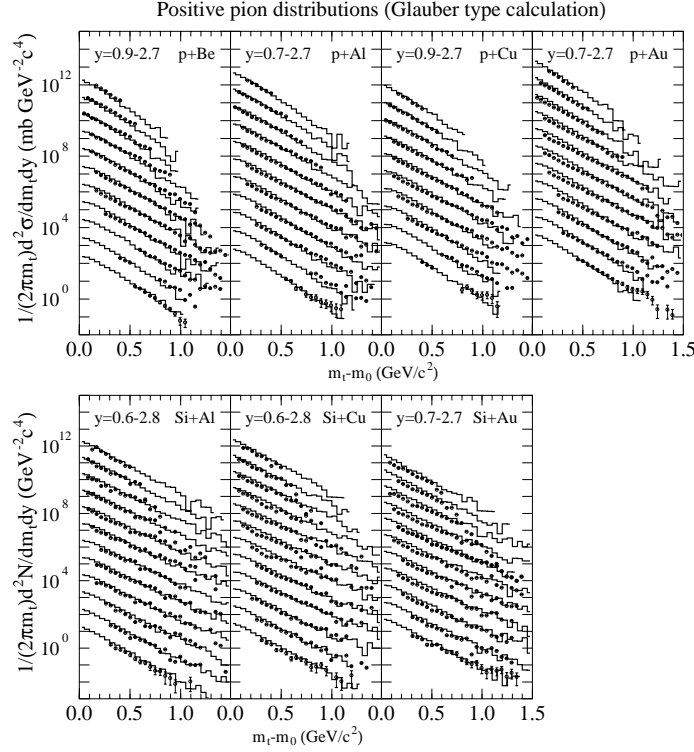

FIG. 19.   Same as Fig. 17, but the histograms show the results obtained from the Glauber type calculations without any rescattering among produced particles.
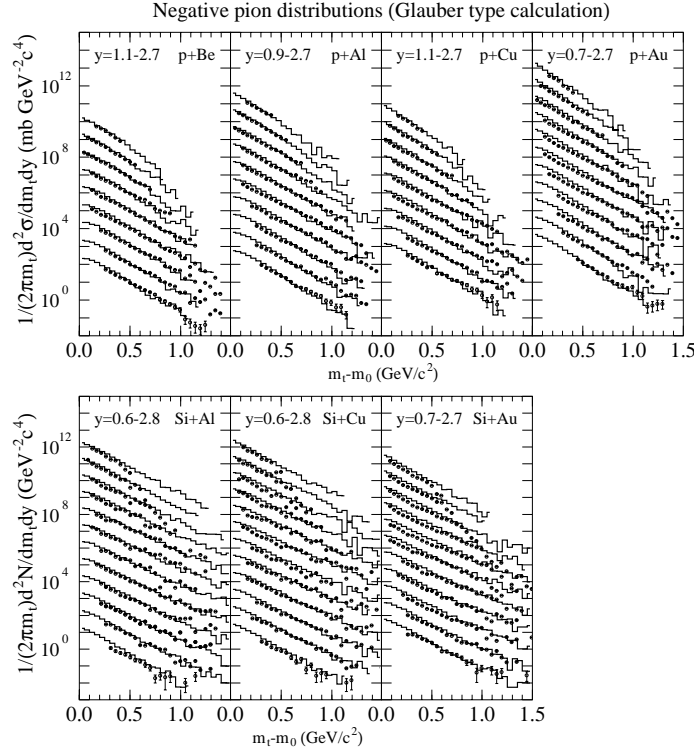
Negative pion distributions (Glauber type calculation)

FIG. 20. Same as Fig. 18, but the histograms show the results obtained from the Glauber type calculations without any rescattering among produced particles.
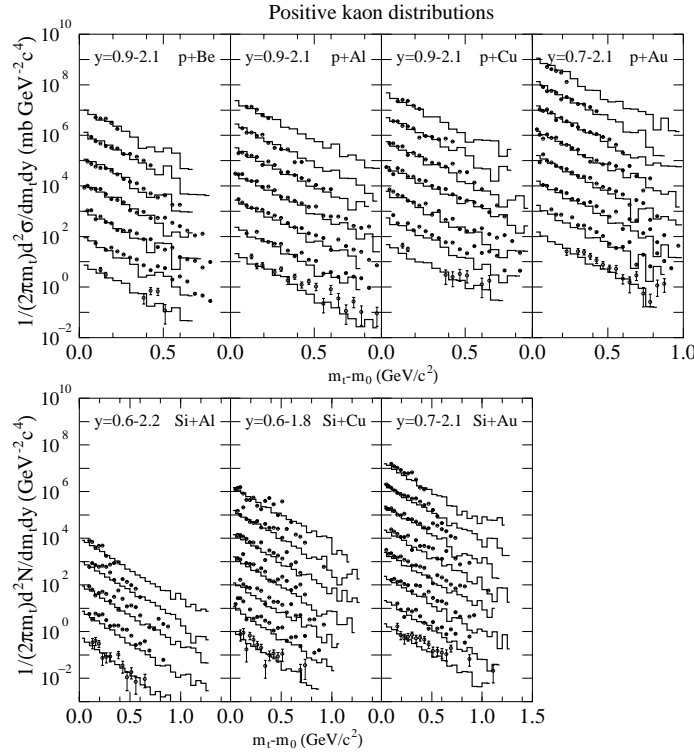
Positive kaon distributions

FIG. 21. Comparison of the invariant transverse momentum spectra of K^+ between the cascade model and the experimental data of [39,40] in p+Be ($0.9 \leq y \leq 2.1$ with bin size 0.2), p+Al ($0.9 \leq y \leq 2.1$ with bin size 0.2), p+Cu ($0.9 \leq y \leq 2.1$ with bin size 0.2), p+Au ($0.7 \leq y \leq 2.1$ with bin size 0.2), Si+Al ($0.6 \leq y \leq 2.2$ with bin size 0.2), Si+Cu ($0.6 \leq y \leq 1.8$ with bin size 0.4) and Si+Au ($0.7 \leq y \leq 2.1$ with bin size 0.2) collisions at 14.6GeV/c. The spectra are increased by a factor of 10 from bottom to upper.
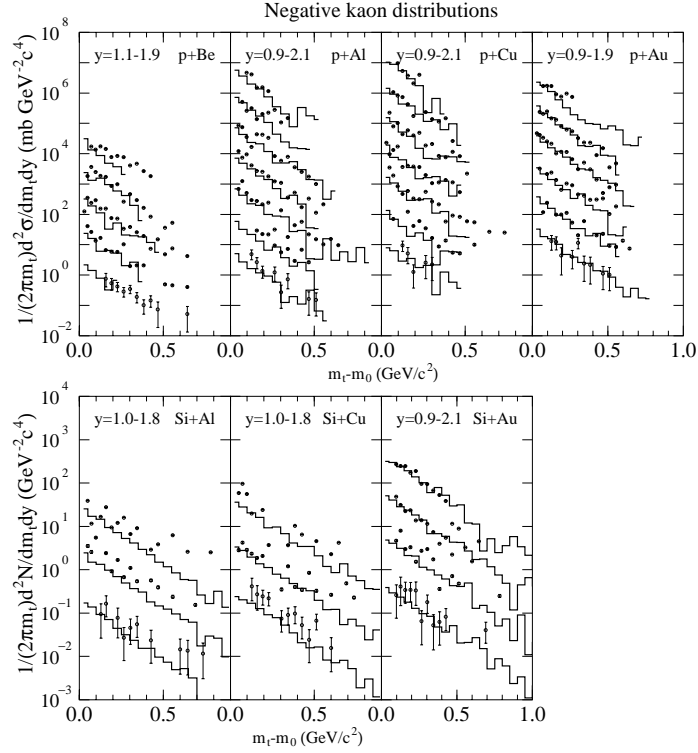
Negative kaon distributions

FIG. 22. Comparison of the invariant transverse momentum spectra of K^- in p+Be ($1.1 \leq y \leq 1.9$ with bin size 0.2), p+Al ($0.9 \leq y \leq 2.1$ with bin size 0.2), p+Cu ($0.9 \leq y \leq 2.1$ with bin size 0.2), p+Au ($0.9 \leq y \leq 1.9$ with bin size 0.2), Si+Al ($1.0 \leq y \leq 1.8$ with bin size 0.4), Si+Cu ($1.0 \leq y \leq 1.8$ with bin size 0.4) and Si+Au ($0.9 \leq y \leq 2.1$ with bin size 0.4) collisions at 14.6GeV/c. The spectra are increased by a factor of 10 from bottom to upper.

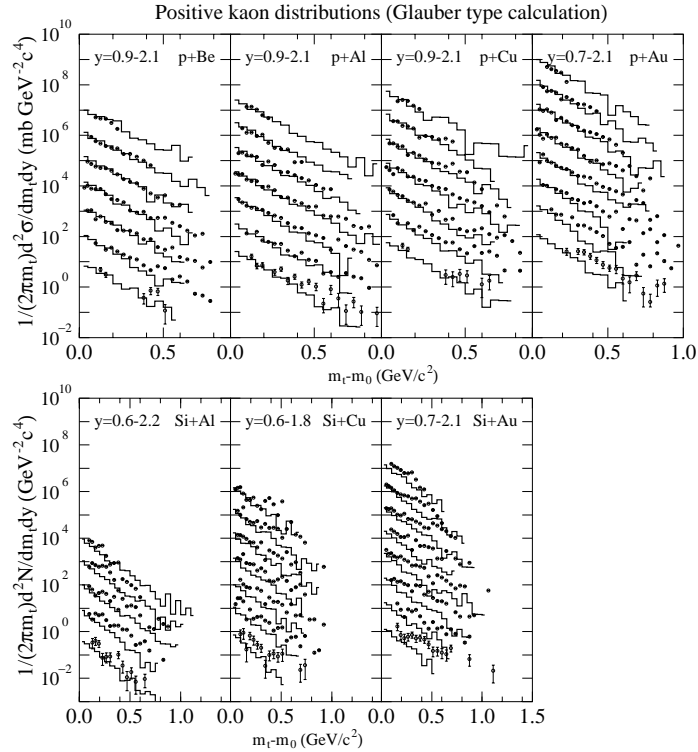## Positive kaon distributions (Glauber type calculation)

FIG. 23. Glauber type calculations of invariant cross sections of K^+ for p+Be, p+Al, p+Cu, p+Au, Si+Al, Si+Cu and Si+Au reactions at 14.6GeV/c. in comparison to the E802 data from [39,40]. The meaning of figure is the same as Fig. 21.
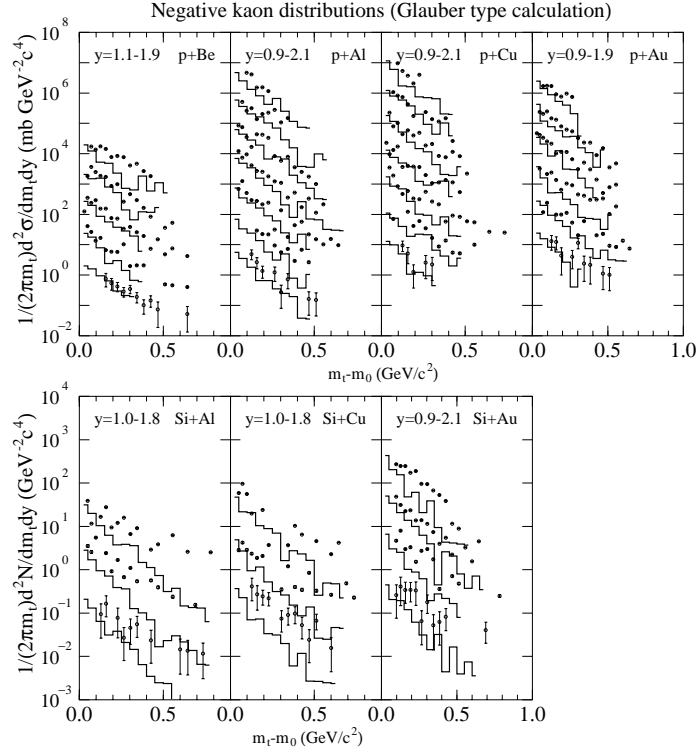
21

FIG. 24. Glauber type calculations of invariant cross sections of K^- for p+Be, p+Al, p+Cu, p+Au, Si+Al, Si+Cu and Si+Au reactions at 14.6GeV/c. in comparison to the E802 data from [39,40]. The meaning of figure is the same as Fig. 22.

Let us study the kaon and anti-kaon transverse mass spectra of E802. The calculated transverse mass distributions of K^+ and K^- in cascade model are compared with the E802 data [39,40] in Figs. 21 and 22. Figures 23 and 24 are the results with the Glauber type calculations for K^+ and K^- invariant transverse momentum distributions. We find more significant differences between the cascade and Glauber results of kaon productions than those in proton and pion spectra. This fact shows the importance of the rescattering: As discussed in II D, some of the exoergic MB reactions, which involve resonances, have very large strangeness production cross sections, and they contribute to K and $\bar{K}$ productions, especially in heavy ion reactions [12,31]. Enhancements due to these meson rescattering are clearly seen in K^+ and K^- spectra, except for the reactions of p+Be and p+Al, because there is no meson-baryon collision in Glauber type calculation.
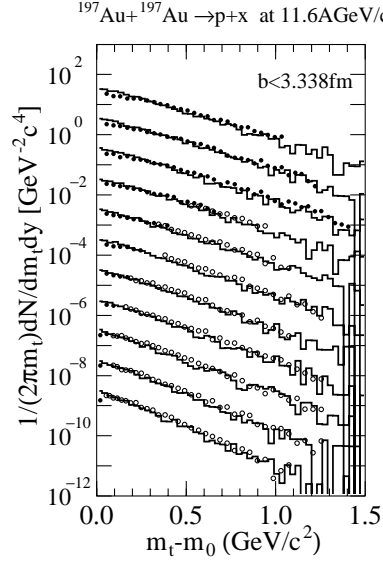
B. Au+Au COLLISIONS

^{197}Au+^{197}Au →p+x at 11.6AGeV/c

FIG. 25. The result of Cascade model calculation of transverse mass distributions of protons for central Au+Au collision at 11.6GeV/c in different rapidity intervals. The spectra are scaled down by a factor of 10 successively from upper corresponds to the c.m. rapidity $y = 0.05$ to lower spectrum of $y = 1.05$ with the bin width of 0.1. Impact parameter is distributed from 0 to 3.338fm. Data are from Ref. [41].

We continue our comparison to E866 experimental data [41] with the truly heavy ion collision Au+Au at 11.6AGeV. Our cascade model calculation with impact parameter $b \leq 3.338$fm is compared to E866 data [41] in Fig. 25 from c.m. rapidity of $y = 0.05$ to $y = 1.05$ with the rapidity bin of 0.1 scaled down by a factor of 10 from the top to the bottom spectrum. The cascade model results show good agreement with the data at the transverse mass above 0.2GeV/c^2. The cascade model, however, overpredicts again the proton spectrum in the low transverse momentum region.
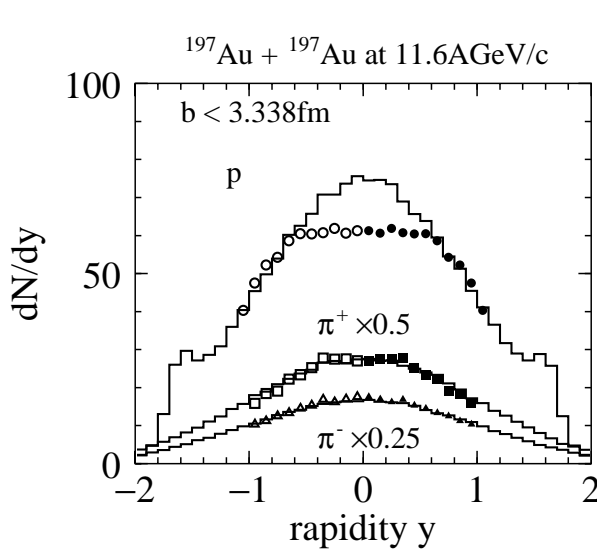

FIG. 26. Comparison of rapidity distributions of protons (circles), positive pions (squares) and negative pions (triangles) between experimental data [41] and cascade model calculations (histograms) for central Au+Au collision at 11.6GeV/c. The data for positive pions is scaled down by a factor of 0.5 and for negative pions 0.25. In cascade calculations, impact parameter is distributed from 0 to 3.338fm.
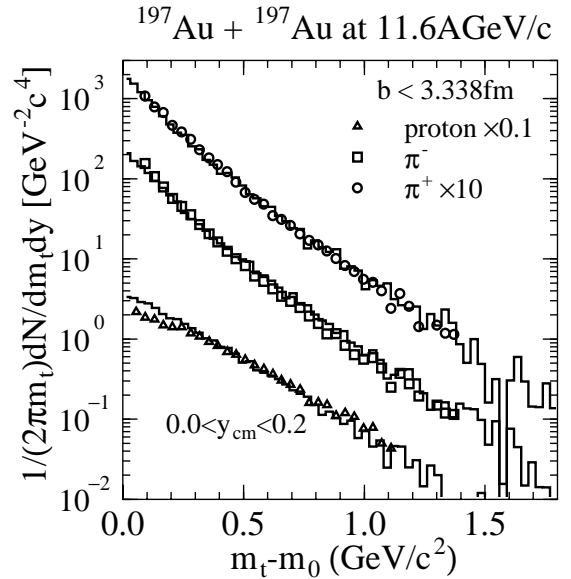

FIG. 27. Transverse mass distributions of protons and pions for central Au+Au collision at 11.6GeV/c. The triangles represent the data of protons scaled by a factor of 0.1 squares correspond to π^- data and circles π^+ data scaled by a factor of 10 from from Ref. [41]. Histograms represent the results from Cascade model with impact parameter $b \leq 3.338$fm.

In Figs. 26 and 27, we compare the cascade model results with the experimental data by E802 collaboration [41] in central Au+Au collisions. Pion multiplicities are in good agreement with data as well as the slopes of both π^+ and π^-. However, the present cascade model does not describe the suppression of protons having low transverse momenta, and consequently it gives stronger stopping of proton than the data. This proton rapidity spectrum for central Au+Au collisions shows a similar amount of stopping as those with other cascade models like RQMD [12], ARC [16] and ART [17]. In addition, Glauber type calculation gives the same results for the proton rapidity distribution. Therefore, this defect is not a consequence of the cascade model. Since the deviation of the transverse mass spectrum of heavy hadrons from a single exponential behavior is generally considered as a result of the radial flow, it may be influenced by the nuclear mean field. In fact, it has been found in the works of RQMD [14] and ART [17] nuclear mean field significantly reduces maximum baryon densities of the hadronic matter, and consequently the midrapidity protons becomes small.

In this work, we have assumed that the elastic and inelastic cross sections involving baryon resonances, except for the de-excitation processes to NN, are the same as that in NN channel at the same c.m. momentum. However, since the de-excitation cross sections are enhanced due to the generalized detailed balance as explained in Section II C, if other cross sections is smaller than those of NN, stopping power may be reduced.

C. Mass dependence of the collision dynamics

In this section, we study the mass dependence of the collision dynamics within the hadronic cascade model. First we present the cascade model results of BB, MB and MM collision number as a function of system mass $(A+B)$ in comparison to that of Glauber type calculations.
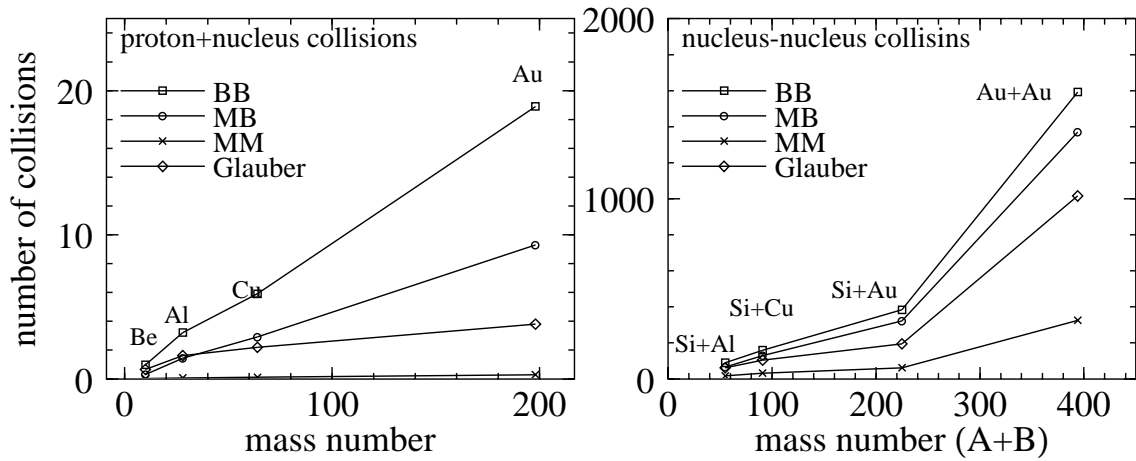

FIG. 28. Mass dependence of number of BB (open squares), MB (open circles) and MM (open crosses) collisions obtained from cascade model calculations and Glauber type calculations (open diamonds) for p+A collisions in the left panel and for Si+A and Au+Au collisions (right panel).

Figure 28 displays the total collision number of BB (open squares) and MB (open circles) and MM (open crosses) obtained from cascade calculation together with Glauber type calculation (open diamonds) for the p+A (left panel) and Si+A (right panel) collisions. When system becomes bigger, BB collisions are much more frequent in cascade model than in the Glauber predictions even in the proton induced collisions. This indicates that there are successive nucleon cascading in the nuclear medium in the cascade model picture. It is interesting to see that the number of BB and MB collisions are almost the same in heavy ion collisions. This seems to be the origin of the pion number suppression, the increase in proton transverse momentum slope, and the increase in kaon yield.
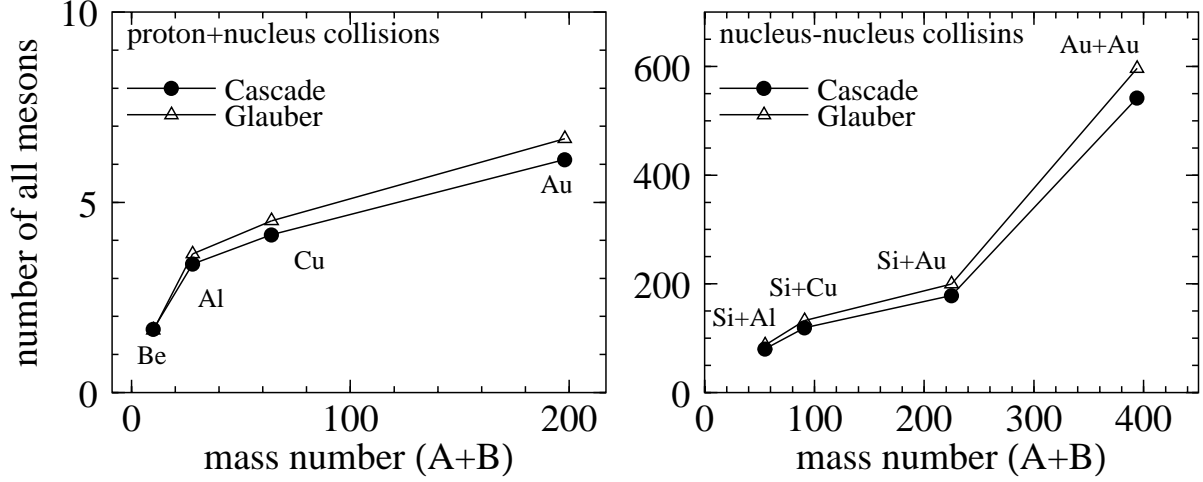
24

FIG. 29. Mass dependence of number of total mesons from cascade model calculations (full circles) and Glauber type calculations (full triangles) for Si+A (A=Al, Cu, Au), Au+Au collisions (right panel) and for p+A (A=Be, Al, Cu, Au) collisions (left panel). Meson multiplicity is reduced by including rescattering.

Indeed we can see the reduction of produced pion multiplicity in cascade model compared to the Glauber type calculations as shown in Fig. 29 where the number of total produced mesons are plotted as a function of system mass number. Pions are absorbed mainly in the two-step processes in the cascade model. For example, the most important pion absorption path at AGS energies is

$$\pi N \to \Delta , \qquad N\Delta \to NN . \tag{39}$$

Therefore, large number of BB and MB collisions are necessary to describe appropriate pion absorptions.
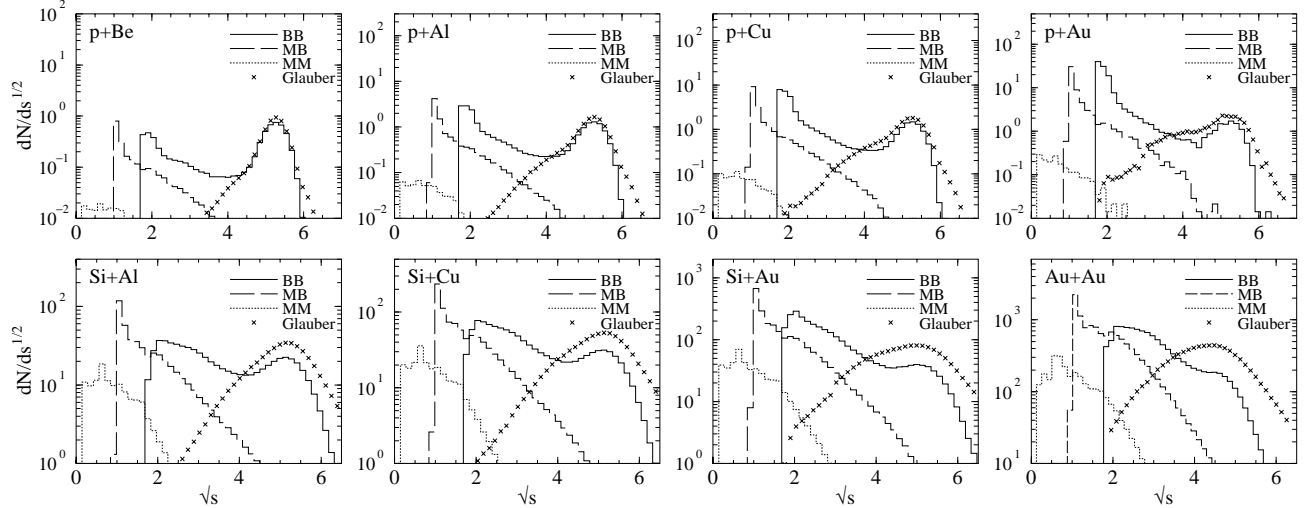

FIG. 30. Collision spectrum of BB (full lines), MB (dashed lines) and MM (dotted lines) collisions from the cascade model calculations and Glauber type calculations (crosses) for the p+Be, p+Al, p+Cu, p+Au, Si+Al, Si+Cu, Si+Au and Au+Au collisions at AGS energies.

In order to get more detailed information on the mass dependence of the collision dynamics at AGS energies, we display in Fig. 30 the colliding energy spectrum of BB, MB and MM given by the cascade model together with

25

those from the Glauber typer calculations. The BB collision distributions as a function of invariant mass are very different between the cascade model and the Glauber type model. The Glauber type calculations predict the collisions which are spread around the initial NN c.m. energy, while the BB collisions occur at all available collision energies in the cascade model. In both p+A and A+B reactions, the MB collisions are pronounced in the resonance region ($\sqrt{s} \leq 2$GeV). It is interesting to note that in p+Au system, the number of low energy BB collision is much larger than that of p+Be, p+Al and p+Cu systems. In A+B systems (bottom of Fig. 30), collision number grows very quickly, however, the shape of the collision spectrum is similar in all the systems.

IV. SUMMARY

We have systematically studied the system mass dependence of the particle distributions at AGS energies with a newly developed cascade model (JAM1.0). The cascade model is shown to provide a good description of the observed data for various combination of projectile and target without any change of model parameters. The effect of rescattering of produced particles and nucleon cascading are found to be important to explain both the pion yield and the transverse slope, which are demonstrated by comparing the cascade model results with the Glauber type calculations. Those effects increase the transverse momentum slopes of protons and pions, and reduce the pion yield. The importance of the rescattering among particles is more visible in kaon spectra.

One of the problems in the hadronic cascade model JAM is that it gives much larger stopping of the protons in nucleus-nucleus collisions. This large stopping is not the consequence of the rescattering because Glauber type calculation also gives the same amount of baryon stopping. This problem of strong baryon stopping in cascade models has been reported that proton spectra can be fitted by the inclusion of nuclear mean field in RQMD [14] and ART [17].

Another possible solution may be to suppress the cross sections such as $\sigma(N_1^* N_2^* \to N_3^* N_4^*)$, which is assumed to be the same as that in NN ingoing channel at the same c.m. momentum in a present model. These interactions among resonances become important at AGS energies where we have sufficiently dense matter in heavy ion collisions, and the baryon stopping is sensitive to the cross sections in the resonance ingoing reactions. In fact, we have checked that if resonance-resonance (BB) cross sections are reduced from nucleon-nucleon cross section, we get less proton stopping than the present results. Detailed study in this line will be interesting.

ACKNOWLEDGMENTS

[1] B. Andersson, G. Gustafson and H. Pi, *Z. Phys.* C **57**, 485 (1993); H. Pi, *Comp. Phys. Comm.* **71**, 173 (1992).
[2] Sa Ben-Hao and Tai An, *Comp. Phys. Comm.* **90**, 121 (1995); *Phys. Rev.* C **55**, 2010 (1997); *Phys. Lett.* B **399**, 29 (1997); *Phys. Lett.* B **409**, 393 (1997).
[3] K. Werner, *Z. Phys.* C **42**, 85 (1989); *Phys. Rep.* **232**, 87 (1993).
[4] X. N. Wang and M. Gyulassy, *Phys. Rev.* D **44**, 3501 (1991); X. N. Wang, *Phys. Rep.* **280**, 287 (1997); X. N. Wang and M. Gyulassy, *Comp. Phys. Comm.* **83**, 307 (1994); *http://www-nsdth.lbl.gov/~xnwang/hijing/*.
[5] A. Capella, U. Sukhatme, C.-I. Tan and J. Tran Thanh Van, *Phys. Rep.* **236**, 225 (1994).
[6] A. Shor and R. Longacre, *Phys. Lett.* B **218**, 100 (1989).
[7] S. Jeon and J. Kapusta, *Phys. Rev.* C **56**, 468 (1997).
[8] K. Geiger, *Phys. Rep.* **258**, 238 (1995); *Comp. Phys. Comm.* **104**, 70 (1997); *http://penguin.phy.bnl.gov/~klaus/*.
[9] B. Zhang, *Comp. Phys. Comm.* **109**, 70 (1997); *http://nt1.phys.columbia.edu/people/bzhang/ZPC/zpc.html*; B. Zhang and Y. Pang, *Phys. Rev.* C **56**, 2185 (1997); B. Zhang, M. Gyulassy and Y. Pang, *Phys. Rev.* C **58**, 1175 (1998).
[10] K. Geiger, *Nucl. Phys.* **A638**, 551c (1998); D. K. Srivastava and K. Geiger, *Phys. Lett.* B **422**, 39 (1998); K. Geiger and B. Mueller, *Heavy Ion Phys* **7**, 207 (1998); K. Geiger and D. K. Srivastava, *Phys. Rev.* C **56**, 2718 (1997): K. Geiger and R. Longacre, *Heavy Ion Phys* **8**, 41 (1998).
[11] H. Sorge, H. Stöcker and W. Greiner, *Annals Phys.* **192**, 266 (1989); H. Sorge, A. von Keitz, R. Mattiello, H. Stöcker and W. Greiner, *Z. Phys.* C **47**, 629 (1990).

[12] H. Sorge, R. Mattiello, A. Jahns, H. Stöcker and W. Greiner, *Phys. Lett.* B **271**, 37 (1991); H. Sorge, L. Winckelmann, H. Stöcker and W. Greiner, *Z. Phys.* C **59**, 85 (1993).

[13] H. Sorge, *Phys. Rev.* C **52**, 3291 (1995).

[14] H. Sorge, R. Mattiello, H. Stöcker and W. Greiner, *Phys. Rev. Lett.* **68**, 286 (1992); R. Mattiello, H. Sorge, H. Stöcker and W. Greiner, *Phys. Rev.* C **55**, 1443 (1997).

[15] L. Bravina, L.P. Csernai, P. Levai, and D. Dtrottman, *Phys. Rev.* C **51**, 2161 (1994).

[16] Y. Pang, T. J. Schlagel, S. H. Kahana, *Nucl. Phys.* **A544**, 435c (1992); *Phys. Rev. Lett.* **68**, 2743 (1992); S. H. Kahana, D. H. Kahana, Y. Pang, and T. J. Schlagel, *Annu. Rev. Part. Sci.* **46**, 31 (1996).

[17] B. A. Li and C. M. Ko, *Phys. Rev.* C **52**, 2037 (1995). *Phys. Lett.* B **382**, 337 (1996); *Nucl. Phys.* **A630**, 556 (1998); *Phys. Rev.* C **58**, R1382 (1998); B. A. Li, C.M. Ko, and G.Q. Li, *Phys. Rev.* C **54**, 844 (1996).

[18] W. Ehehalt and W. Cassing *Nucl. Phys.* **A602**, 449 (1996); J. Geiss, W. Cassing and C. Greiner, nucl-th/9805012.

[19] L.A. Winckelmann, S.A. Bass, M. Bleicher, M. Brandstetter, A. Dumitru, C. Ernst, L. Gerland, J. Konopka, S. Soff, C. Spieles, H. Weber, C. Hartnack, J. Aichelin, N. Amelin, H. Stöcker and W. Greiner, *Nucl. Phys.* **A610**, 116c (1996); nucl-th/9610033; S.A. Bass, M. Belkacem, M. Bleicher, M. Brandstetter, L. Bravina, C. Ernst, L. Gerland, M. Hofmann, S. Hofmann, J. Konopka, G. Mao, L. Neise, S. Soff, C. Spieles, H. Weber, L.A. Winckelmann, H. Stöcker, W. Greiner, C. Hartnack, J. Aichelin and N. Amelin, *Prog. Part. Nucl. Phys.* **41**, 225 (1998); nucl-th/9803035.

[20] H. Weber, C. Ernst, M. Bleicher, L. Bravina, H. Stöcker and W. Greiner, nucl-th/9808021.

[21] Y. Nara, N. Otuka, A. Ohnishi and T. Maruyama, *Prog. Theor. Phys. Suppl.* **129**, 33 (1997)

[22] T. Sjöstrand, *Comp. Phys. Comm.* **82**, 74 (1994); PYTHIA 5.7 and JETSET 7.4 Physics and Manual. *http://thep.lu.se/tf2/staff/torbjorn/Welcome.html.*

[23] Y. Nara, *Nucl. Phys.* **A638**, 555c (1998).

[24] Particle-Data-Group, *Phys. Rev.* D **54**, (1996).

[25] *Total Cross-Sections for Reactions of High Energy Particles* vol. 12a and vol. 12b edited by A. Baldni, V. Flaminio, W. G. Moorhead and D. R. O. Morrison (Springer-Verlag Berlin 1988).

[26] High-Energy Reactions Analysis Group, CERN Report CERN-HERA 83-01 and 83-02, 1983 (unpublished).

[27] S. Teis, W. Cassing, M. Effenberger, A. Hombach, U. Mosel and Gy. Wolf, *Z. Phys.* A **356**, 421 (1997). M. Effenberger, A. Hombach, S. Teis and U. Mosel, *Nucl. Phys.* **A613**, 353 (1997).

[28] P. Danielewicz and G. F. Bertch, *Nucl. Phys.* **A533**, 712 (1991).

[29] Bao-An Li, *Nucl. Phys.* **A552**, 605 (1993).

[30] Gy. Wolf, W. Cassing, U. Mosel, *Nucl. Phys.* **A552**, 549 (1993).

[31] Y. Nara, A. Ohnishi, T. Harada and A. Engel, *Nucl. Phys.* **A614**, 433 (1997).

[32] K. Goulianos, *Phys. Rep.* **101**, 1983 (169).

[33] A. S. Rosenthal and F. Tabakin, *Phys. Rev.* C **22**, 1980 (711).

[34] K. Niita, S. Chiba, T. Maruyama, T. Maruyama, H. Takada, T. Fukahori, Y. Nakahara and A. Iwamoto, *Phys. Rev.* C **52**, 2620 (1995).

[35] A. Bialas and M. Gyulassy, *Nucl. Phys.* **B291**, 793 (1987).

[36] Bonn-Hamburg-München Collaboration, V. Blobel *et al.*, *Nucl. Phys.* **B69**, 454 (1974)

[37] G. E. Brown, C. M. Ko, Z. G. Wu and L. H. Xia, *Phys. Rev.* C **43**, 1881 (1991).

[38] JAM1.0, source code and its documentation, to be prepared.

[39] E802 Collaboration, T. Abbott, *et al.*, *Phys. Rev.* D **45**, 3906 (1992); Compilation of Relativistic Heavy-Ion Data, *http://www.nndc.bnl.gov/∼hi_data/rhid.html.*

[40] E802 Collaboration, T. Abbott, *et al.*, *Phys. Rev.* D **50**, 1024 (1994); Compilation of Relativistic Heavy-Ion Data, *http://www.nndc.bnl.gov/∼hi_data/rhid.html.*

[41] E802 Collaboration, L. Ahle, *et al.*, *Phys. Rev.* C **57**, R466 (1998).